Design and Construction Guidelines for Geosynthetic-Reinforced Soil Bridge Abutments with a Flexible Facing: Appendix C--Verification of the Analytical Model

DETAILS

0 pages | | PAPERBACK
ISBN 978-0-309-43154-5 | DOI 10.17226/21981

AUTHORS

NCHRP Web-Only Document 81 (Project 12-59): Contractor's Final Report—Appendix C

Design and Construction Guidelines for GRS Bridge Abutments with a Flexible Facing: Appendix C—Verification of the Analytical Model

Prepared for:

National Cooperative Highway Research Program

TRANSPORTATION RESEARCH BOARD
OF THE NATIONAL ACADEMIES

Submitted by:

Jonathan T. H. Wu, Kevin Z. Z. Lee,
Sam B. Helwany, and Kanop Ketchart
University of Colorado at Denver
Denver, Colorado

December 2004

ACKNOWLEDGMENT

This work was sponsored by the American Association of State Highway and Transportation Officials (AASHTO), in cooperation with the Federal Highway Administration, and was conducted in the National Cooperative Highway Research Program (NCHRP), which is administered by the Transportation Research Board (TRB) of the National Academies.

THE NATIONAL ACADEMIES

Advisers to the Nation on Science, Engineering, and Medicine

The **National Academy of Sciences** is a private, nonprofit, self-perpetuating society of distinguished scholars engaged in scientific and engineering research, dedicated to the furtherance of science and technology and to their use for the general welfare. On the authority of the charter granted to it by the Congress in 1863, the Academy has a mandate that requires it to advise the federal government on scientific and technical matters. Dr. Ralph J. Cicerone is president of the National Academy of Sciences.

The **National Academy of Engineering** was established in 1964, under the charter of the National Academy of Sciences, as a parallel organization of outstanding engineers. It is autonomous in its administration and in the selection of its members, sharing with the National Academy of Sciences the responsibility for advising the federal government. The National Academy of Engineering also sponsors engineering programs aimed at meeting national needs, encourages education and research, and recognizes the superior achievements of engineers. Dr. William A. Wulf is president of the National Academy of Engineering.

The **Institute of Medicine** was established in 1970 by the National Academy of Sciences to secure the services of eminent members of appropriate professions in the examination of policy matters pertaining to the health of the public. The Institute acts under the responsibility given to the National Academy of Sciences by its congressional charter to be an adviser to the federal government and, on its own initiative, to identify issues of medical care, research, and education. Dr. Harvey V. Fineberg is president of the Institute of Medicine.

The **National Research Council** was organized by the National Academy of Sciences in 1916 to associate the broad community of science and technology with the Academy's purposes of furthering knowledge and advising the federal government. Functioning in accordance with general policies determined by the Academy, the Council has become the principal operating agency of both the National Academy of Sciences and the National Academy of Engineering in providing services to the government, the public, and the scientific and engineering communities. The Council is administered jointly by both the Academies and the Institute of Medicine. Dr. Ralph J. Cicerone and Dr. William A. Wulf are chair and vice chair, respectively, of the National Research Council.

The **Transportation Research Board** is a division of the National Research Council, which serves the National Academy of Sciences and the National Academy of Engineering. The Board's mission is to promote innovation and progress in transportation through research. In an objective and interdisciplinary setting, the Board facilitates the sharing of information on transportation practice and policy by researchers and practitioners; stimulates research and offers research management services that promote technical excellence; provides expert advice on transportation policy and programs; and disseminates research results broadly and encourages their implementation. The Board's varied activities annually engage more than 5,000 engineers, scientists, and other transportation researchers and practitioners from the public and private sectors and academia, all of whom contribute their expertise in the public interest. The program is supported by state transportation departments, federal agencies including the component administrations of the U.S. Department of Transportation, and other organizations and individuals interested in the development of transportation.
www.TRB.org

www.national-academies.org

APPENDIX C
VERFICATION OF THE ANALYTICAL MODEL

The capability of DYNA3D/LS-DYNA for analyzing the performance of segmental facing GRS bridge abutments was critically evaluated. To achieve the purpose of evaluating the analytical tool, it was necessary to compare the analytical results with experimental or field-measured results that involve the critical components of the problem on hand. This means that it is necessary to select closely related case histories of which the measured results are reliable, the placement density and moisture conditions of the fill are well monitored, and the material parameters (stress-strain-strength and volume change behavior of the soil and load-deformation properties of the reinforcement) are well documented. Following an extensive search and careful consideration, five case histories that involved critical components of segmental GRS abutments were selected for the evaluation, including (1) the spread footing experiments by Briaud and Gibbens (1994), (2) the spread footing experiments on reinforced sands by Adams and Collin (1997), (3) the FHWA Turner-Fairbank GRS bridge pier in Virginia, USA (Adams 1997), (4) the "Garden" experimental embankment in France (Gotteland et al. 1997), and (5) the two full-scale GRS bridge abutment loading experiments conducted as part of this study (refer to as "the NCHRP GRS abutment experiment"). It is to be noted that the first two experiments involved spread footings on sand. They were included as a part of the verification study because it was considered important to examine the adequacy of DYNA3D and the extended two-invariant geologic cap model in terms of their capability to predict failure loads of spread footings on un-reinforced and reinforced soils.

Spread Footing Experiments by Briaud and Gibbens (1994)

Five spread footings were load-tested in Briaud and Gibbens' experiments. The footings ranged in size from 1.0 m by 1.0 m to 3.0 m by 3.0 m. All footings were 1.2 m thick and were founded at a depth of 0.76 m in the sand that was 11 m thick. The parameters for the extended two-invariant geologic cap model were deduced from five CPT soundings performed in the vicinity of the footings. The results of the CPT tests were averaged as shown in Figure C-1.

The parameters for the extended two-invariant geologic cap model include the effective stress friction angle (ϕ), over-consolidation ratio (OCR), lateral stress coefficient (K_o), and initial shear modulus (G) and bulk modulus (K). These parameters are function of the cone tip resistance, q_c, and the in-situ effective stresses. The equations needed to calculate these parameters are presented elsewhere (Mayne 2001). The calculated parameters are shown in Figure C-1. The cap model parameters that control volumetric changes are deduced from the triaxial test results presented by Briaud and Gibbens (1994).

The 3-D finite element discretization of the footing problem is shown in Figure C-2. Only ¼ of the configuration is discretized because of symmetry. The load is applied gradually at the same rate as field tests. The strength of the extended two-invariant geologic cap model via DYNA3D is its capability to

analyze failure and post failure conditions of soils. Figure C-3, for example, shows the initiation of a three-dimensional shear band (localized shear) under the footing during load application indicating that the footing is on the verge of failure.

Figures C-4 to C-7 show the measured versus calculated load-displacement curves for the 1.0 m x 1.0 m, 1.5 m x 1.5 m, 2.5 m x 2.5 m, and 3.0 m x 3.0 m footings, respectively. Excellent agreement between measured and calculated displacements is noted in all four cases. This ascertains the capabilities of DYNA3D in predicting settlements under working stress conditions and in predicting failure conditions. This successful numerical simulation can also be attributed to the extensive field and laboratory soil testing program that was performed prior to the spread footing experiments. The results of that testing program were used to obtain accurate and representative model parameters for the numerical analysis.

Spread Footing Experiments by Adams and Collin (1997)

Adams and Collin's field experiments involved load-testing spread footings on compacted sand with and without geosynthetic reinforcement. The tests were performed in a test pit measuring 5.4-m wide, 6.9-m long, and 6-m deep. Four square footings with various sizes were tested. The analysis conducted in this study included only the 0.61 m x 0.61 m footing which was founded on the surface of the compacted sand (i.e., $D_f = 0$). The sand used in the experiment was fine concrete mortar sand classified as a poorly graded sand. The test was repeated twice, once without geosynthetic reinforcement, and another with three layers of geosynthetic reinforcement located at depths of 0.15 m, 0.3 m, and 0.45 m below the ground surface. The geosynthetic reinforcement used in the test was a polypropylene biaxial geogrid with an ultimate strength of 34 kN/m, per ASTM D4595.

The finite element discretization of the test configuration is shown in Figure C-8. Only one-quarter of the entire system is discretized because of symmetry. Because of absence of soil element test results, the stress-strain-strength parameters and the volumetric strain behavior of the soil is estimated based on engineering judgment. The relative density of the compacted sand is estimated to be approximately 43% indicating that the internal friction angle of the soil is approximately 27.5º. This friction angle is used to calculate the strength parameter θ used in the cap model. The cap model parameters that control volumetric changes were also estimated based on engineering judgment.

Figure C-9 shows a comparison between measured and calculated displacements of the footing with and without geosynthetic reinforcement. A good agreement between measured and calculated results is noted for the case of unreinforced foundation soil. However, the calculated displacements for the case of the reinforced foundation soil are not in good agreement with the measured displacements. The calculated displacements are within 10-15% error for applied pressures less than 200 kPa. The error increases considerably as the applied pressure increases. This discrepancy between measured and calculated displacements for the case of reinforced foundation soil is caused by the failure

of recognizing the effects of the geosynthetic reinforcing layers on the efficiency of compaction of the reinforced soil. The reinforcement layers restrain the lateral deformation of soil layers during compaction, thus increasing compaction effectiveness. This indicates that for the same compaction effort an unreinforced soil layer will compact less than a reinforced soil layer, i.e., the reinforced soil layer can achieve a greater dry unit weight, therefore, a greater stiffness and strength and less volumetric changes when subjected to external loading. Moreover, and because of the aforementioned lateral restrain effect of the reinforcement layers, a reinforced soil layer may retain greater residual (locked-in) lateral stresses after the vertical stresses exerted by the compaction factory are released.

To ascertain this hypothesis, the analysis of the case of the reinforced foundation soil is repeated but with increasing the internal friction angle of the soil to 27.5º + 5º = 32.5º. This increase of 5º is thought appropriate to account for the increased effectiveness of compaction of the reinforced soil under the same compaction effort. The cap model parameters that control volumetric changes were not altered. A better agreement between measured and calculated displacement is noted in Figure C-9.

The FHWA GRS Pier (Adams 1997)

DYNA3D was used to analyze the 5.4-m high FHWA GRS pier with segmental facing (Adams 1997). A three-dimensional model of the pier was developed as indicated in Figures C-10 and C-11 (¼ of the pier is considered because of symmetry). Several important aspects were considered for a reliable finite element modeling of the test pier: (1) the correct modeling of materials involved, e.g., the elasto-plastic behavior of the backfill soil, and (2) the correct modeling of interfaces between concrete blocks and geosynthetic layers; geosynthetic layers and backfill soil; concrete blocks and backfill soil; and between concrete blocks.

The test pier involved 26 equally-spaced geosynthetic layers (20 cm apart), and the segmental facing consisted of 27 concrete blocks stacked vertically (the analysis assumed no wall batter for simplicity). The soil was discretized into solid hexahedron elements. Each concrete block was discretized into solid hexahedron elements, and each geosynthetic layer was discretized into "thin" solid hexahedron elements. The soil behavior was simulated by an elasto-plastic extended two-invariant geologic cap model (Sandler and Rubin 1979). The concrete blocks were assumed to behave in a linear elastic manner. The geosynthetic reinforcement was assumed to behave in an elastic-plastic manner. The interface between different structural parts of the test pier was carefully simulated utilizing the "sliding interface" available in DYNA3D. The sliding interface is a penalty-function based contact surface which allows sliding between disjointed model parts with separation and friction. Large relative motions are permitted, and Coulomb friction is included. Surfaces may separate and come together in a completely arbitrary fashion -- a feature essential for the current analysis. The friction angle of the crushed Diabase rock backfill is assumed to be 50º. This friction angle is used to calculate the strength

parameter θ used in the cap model. The cap model parameters that control volumetric changes were estimated based on engineering judgment. For simplicity, a preconsolidation pressure (preloading pressure) of 900 kPa is assumed. Only the reloading stage is simulated in the present analysis.

The measured and calculated vertical displacements of the loading pad are compared in Figure C-12. The analytical results, especially in terms of failure load, are in good agreement with the measured results (within a ±10 % error). Calculated displacements are in fair agreement with measured displacements, as expected, since the parameters that control volumetric changes were base on educated assumptions rather than the results of soil element tests. Nevertheless, the calculated ultimate strength is in good agreement with the measured one as indicated above. Figure C-13 shows the distribution of calculated maximum shear strains immediately before failure. Shortly after that there was a sudden increase in shear strains within the soil mass as indicated in Figure C-14. In this figure, the average shear strain in seven elements (marked on Figure C-10) is plotted versus the applied pressure.

The "Garden" GRS Bridge Abutment (Gotteland et al. 1997)

The "Garden" (**G**eotextiles: **A**pplication en **R**enforcement, **E**xperimentation et **N**ormalisation) GRS bridge abutment test was conducted in 1993 by Gotteland et al. (1997) to investigate the capability of GRS segmental walls to support bridge loads transmitted via spread footings. The "Garden" experiment involved a 4.35 m high segmental wall with a 80º batter. The segmental wall included 15 courses of 30 cm-thick concrete blocks. The geosynthetic reinforcement used was a non-woven geotextile with an ultimate strength of 25 kN/m at 30% strain. The reinforcement was a low strength geotextile, with a stiffness of 95 kN/m. The vertical spacing of the reinforcement was 60 cm except at the top and bottom of the segmental wall, as shown in Figure C-15. The embedded length of the geosynthetic layer was 2.5 m except for the top two layers that were 3 m long. The backfill soil used was a compacted fine sand with an estimated friction angle of 36º. The 1-m wide spread footing was positioned in a way that the distance between the back of the segmental wall and the foundation's front edge was 1.0 m (i.e., clear distance = 1.0 m). The footing was brought to failure using hydraulic actuators with an external support system.

A three-dimensional/plane strain finite element model of the "Garden" GRS bridge abutment was constructed (Figure C-16) and analyzed using DYNA3D. The soil was simulated utilizing an extended two-invariant geologic cap model. It is noteworthy that in the cap model, volumetric response is elastic until the stress point comes in contact with the cap surface. Thereafter, plastic volumetric strain (compaction) is generated at a rate controlled by the hardening law. Thus, in addition to controlling the amount of dilatancy, the introduction of the cap surface adds more experimentally observed response characteristic of geological materials to the model. The use of this model is very important to the analysis of GRS abutments where predicting the failure conditions is of special interest. This model makes it possible to predict the ultimate abutment loads that will cause different modes of failure, including bearing capacity failure, segmental

facing failure, and/or geogrid failure. The predicted ultimate loads can then be used to assess proper safety factors.

Figure C-17 shows the calculated and measure displacements of the spread footing. Excellent agreement is noted in the figure especially in terms of ultimate bearing capacity of the footing. Failure occurred at a contact pressure of approximately 140 kPa. This rather low bearing capacity is attributed to several factors: (1) the geotextile used is of lower stiffness and strength, (2) geotextile spacing was rather high (60 cm) except near the top and bottom of the wall, (3) geotextile length was also rather small (57% of wall height except for the top two layers), (4) the clearance between the footing and the facing was rather high (1 m), and (5) the test did not include an approach fill behind the abutment which would be normally utilized in a bridge application. Nevertheless, the "Garden" experiment is an excellent test to calibrate and to ascertain the capabilities of the numerical model.

Figure C-18 shows the distribution of the maximum shear strength within the soil mass at failure (footing pressure = 140 kPa). A distinct shear band (localized strain) is noted beneath the spread footing. Figure C-19 shows how the post-failure shear zone (footing pressure = 190 kPa) expanded towards the segmental facing creating a circular wedge that is very similar in shape to the slip surface observed in the "Garden" experiment. Figure C-20 shows the distribution of the horizontal displacements in the "Garden" experiment corresponding to a footing pressure of 190 kPa. It is noted from the figure that the soil wedge has displaced relative to the rest of the backfill which remained nearly stationary during load application.

Figure C-21 shows a comparison between measured and calculated strains in geotextile layers 3, 5, 7, and 9 at a footing pressure of 190 kPa. Good agreement is noted in the figure both in trend and maximum strain values. Figure C-22 shows a comparison between measured and calculated lateral displacement of the segmental facing. Again, good agreement is noted.

The NCHRP GRS Test Abutments

Two full-scale loading tests, referred to as the NCHRP test abutments, were conducted in the course of this study. The configuration of the NCHRP GRS bridge abutment experiment is depicted in Figure C-23. The experiment includes two test sections: the Amoco test section and the Mirafi test section. The main features of the two test sections are summarized in Table C-1. A detailed description of the full-scale experiments is given in Chapter 2.

The results of conventional triaxial compression tests conducted on reconstituted backfill soil specimens (with the same dry unit weight and moisture content in the as-compacted condition in the full-scale experiments) are shown in Figure C-24. Also shown in Figure C-24 are the results of a hydrostatic compression test conducted on a reconstituted soil specimens.

The Amoco test section utilized Amoco 2044, a woven polypropylene geotextile, as reinforcement; whereas the Mirafi test section utilized Mirafi 500x, also a woven polypropylene geotextile, as reinforcement. The two geotextiles differ in stiffness and strength. The ultimate tensile strength of Amoco 2044 and

Mirafi 500x are 70 kN/m and 21 kN/m, respectively, per ASTM D4595. Figures C-25 and C-26 show the results of uniaxial tension tests conducted on Amoco 2044 and Mirafi 500x, respectively.

A three-dimensional plane strain finite element analysis of the NCHRP GRS bridge abutment was carried out using DYNA3D. The backfill was simulated utilizing an extended two-invariant geologic cap model. The use of the elasto-plastic model is important for the analysis of GRS abutments where predicting the failure conditions is of particular interest. The model is described in the following section.

The behavior of the geosynthetic reinforcement was simulated using an elasto-plastic model with provision of failure. The use of the elasto-plastic model with provision of failure is needed for analyses that may involve failure of the geosynthetic reinforcement. In this model, the geosynthetic reinforcement will lose its tensile resistance immediately after failure has occurred.

The strength parameters θ and α of the cap model were obtained directly from a $\sqrt{J_{2D}}$ versus J_1 plot based on the results of several triaxial compression tests at failure, as illustrated in Figure C-27. The results of the hydrostatic compression test were used to evaluate the parameters D and W. Figure C-28 shows the results of the hydrostatic compression test of the backfill used in the test sections. The plastic volumetric strain versus pressure curve depicted in the Figure was obtained from the total volumetric strain curve by subtracting the elastic strains from the corresponding total volumetric strain. The parameter W (W = 0.023) represents the asymptote value of the plastic volumetric strain curve as illustrated in Figure C-28. The parameter D=0.00087 kPa^{-1} was obtained by a try-and-error approach until a best fit curve was achieved.

The parameter X_0 is the first invariant of the effective stress tensor corresponding to the initial yield cap (see Figure C-29). This parameter was used to account for pre-stress of the backfill caused by compaction. An estimated vertical stress of 8.0 kPa, due to the 3000-N weight compaction machine, was used to calculate the at-rest lateral stress of the soil. The parameter X_0 (X_0 = 15.9 kPa) was then calculated by summing the three principal stresses, i.e., the vertical stress and the two at-rest lateral stresses [$X_0 = \sigma_v(1 + 2K_0)$, where σ_v is the vertical stress and K_0 is the coefficient of lateral earth pressure at rest].

A summary of the elasto-plastic soil parameters is given in Table C-2. These parameters were used in finite element simulation, using DYNA3D, of three triaxial compression tests at three different confining pressures conducted on the backfill for the two test sections. The finite element simulation results were in good agreement with triaxial test results, as shown in Figure C-30.

The Amoco Test Section

A three-dimensional/plane strain finite element model of the NCHRP test abutments was constructed (see Figures C-31 and C-32) and analyzed using DYNA3D. The soil was simulated by utilizing an extended two-invariant elasto-plastic cap model because the prediction of the failure conditions was of special interest. The model parameters used for the analysis are listed in Table C-2.

The behavior of the geosynthetic reinforcement was simulated by using an elasto-plastic model with provision of failure. The elasto-plastic material parameters and the failure parameters of the geosynthetic reinforcement used in the two test sections are given in Table C-3. The use of the elasto-plastic model with failure is deemed important for analyses that may involve geosynthetic failure. It is to be noted that when an elasto-plastic model without provision of failure is used, the geosynthetic reinforcement will tend to sustain erroneously appreciable tensile loads even after the tensile strains become in excess of failure strains (as in the analysis of the Mirafi test section).

Three-dimensional eight-node continuum elements were used to model the soil, the modular block facing, and the geosynthetic reinforcement. Interface elements were used between the modular blocks and reinforcement, and between blocks and backfill soil. The interface element was a “penalty” type element that allows sliding with friction and separation. A friction coefficient of 0.3 was assumed between all contact surfaces.

Figure C-33 shows the displacement field of the Amoco test section at 814 kPa sill pressure. This pressure was the loading at which the Amoco test was terminated (without encountering wall failure). Figure C-34 shows the calculated and measured displacements of the block facing at three sill pressures: 207 kPa, 475 kPa, and 814 kPa. Reasonably good agreement between measured and calculated results is noted in the figure.

Figure C-35 shows the calculated and measured sill vertical displacement. The measured displacements are in good agreement with the calculated values. At 814 kPa sill pressure, the difference between calculated and measured displacements is approximately 12%.

The Mirafi Test Section

Figure C-36 shows the displacement field of the Mirafi test section at 414 kPa sill pressure. This pressure was the loading at which the Mirafi test section was terminated because of excessive deformation. Figure C-37 shows the calculated and measured displacements of the block facing at three sill pressures: 214 kPa, 317 kPa, and 414 kPa. Reasonable agreement between measured and calculated results is noted in the figure.

Figure C-38 shows the calculated and measured sill vertical displacements. The measured displacements are in agreement with the calculated settlements. More importantly, however, the calculated displacements of the sill clearly indicate that failure was occurring at approximately 370 kPa sill pressure, as can be seen in Figure C-38. This is in agreement with the measured sill pressure at “failure” of 414 kPa, with approximately 10% difference.

The finite element analysis of the Mirafi test section indicates that “failure” (noted in Figure C-38 at a sill pressure of 370 kPa) occurred immediately after the tensile rupture of the geosynthetic reinforcement at several locations, notably near the top of the wall at the reinforcement-block interface. Figure C-39 shows the behavior of two geosynthetic reinforcement elements A and B located in the two uppermost reinforcement layers adjacent to the facing blocks. Note the total loss of tensile capacity after reinforcement failure had occurred. The total loss of

tensile capacity was modeled using an elasto-plastic model with provision of failure, as described earlier.

It is noteworthy that the analytical model with DYNA3D is capable of predicting the ultimate load condition that may involve one or more modes of failure, including bearing capacity failure, segmental facing failure, and/or reinforcement failure.

Table C-1 Main features of the NCHRP test abutments

	Amoco Test Section	**Mirafi Test Section**
Abutment height	4.65 m (15.25 ft)	4.65 m (15.25 ft)
Sill	0.9 m x 4.5 m (3 ft x 15 ft)	0.9 m x 4.5 m (3 ft x 15 ft)
Sill clear distance	0.15 m (6 in.)	0.15 m (6 in.)
Reinforcement length	3.15 m (10 ft)	3.15 m (10 ft)
Facing blocks (concrete)	194 mm x 194 mm x 397 mm (7.625 in. x 7.625 in. x 15.625 in.)	194 mm x 194 mm x 397 mm (7.625 in. x 7.625 in. x 15.625 in.)
Vertical reinforcement spacing	0.2 m (8 in.)	0.2 m (8 in.)
Reinforcements	Amoco 2044: a woven polypropylene geotextile with $T_{@\ \varepsilon = 1.0\%}$ = 12.3 kN/m (70 lb/in.) and T_{ult} = 70 kN/m (400 lb/in.), per ASTM D4595, in the cross-machine direction.	Mirafi 500x: a woven polypropylene geotextile with T_{ult} = 21 kN/m (120 lb/in.), per ASTM D4595, in the cross-machine direction.
Backfill	For both test sections: a non-plastic silty sand (SP-SM, per USC System) Gradation: Percent passing 0.75-in. sieve = 100% Percent passing No.40 sieve = 59% Percent passing No.200 sieve = 8.5% Compaction Test, per AASHTO T-99: Maximum dry unit weight = 18.3 kN/m^3 (116.5 lb/ft^3) Optimum moisture content = 11.5% Standard Direct Shear Test (on the portion passing No. 10 or 2 mm sieve, at 95% maximum dry unit weight per AASHTO T-99; specimen size: 60 mm by 60 mm) Cohesion = 14 kPa (2 psi) Internal friction angle = 34.8° Large-size Direct Shear Test (at 99% maximum dry unit weight & 1.5% wet of optimum, per AASHTO T-99; specimen size: 300 mm by 300 mm) Cohesion = 0 kPa Internal friction angle = 36.5° Drained Triaxial Test (on the portion passing 9.5 mm or 3/8 in. sieve; at 99% maximum dry unit weight & 1.5% wet of optimum, per AASHTO T-99; specimen size: 150 mm diameter, 300 mm high) Cohesion = 20 kPa (3 psi) Internal friction angle = 37.3°	

Table C-2 Elasto-plastic soil parameters

Cap Model Parameters	
K (kPa)	52,190
G (kPa)	24,087
α (kPa)	10
θ	0.2925
R	4.0
D (kPa^{-1})	0.00087
W	0.023
X_0 (kPa)	15.93

Table C-3 Elasto-plastic reinforcement parameters

Reinforcement	G (kPa)	σ_0 (kPa)	E_T (kPa)	ε^p_f	K (kPa)
Amoco test section	18,989	1,177	45,100	0.02983	56,070
Mirafi test section	11,472	157	17,073	0.02971	24,860

.

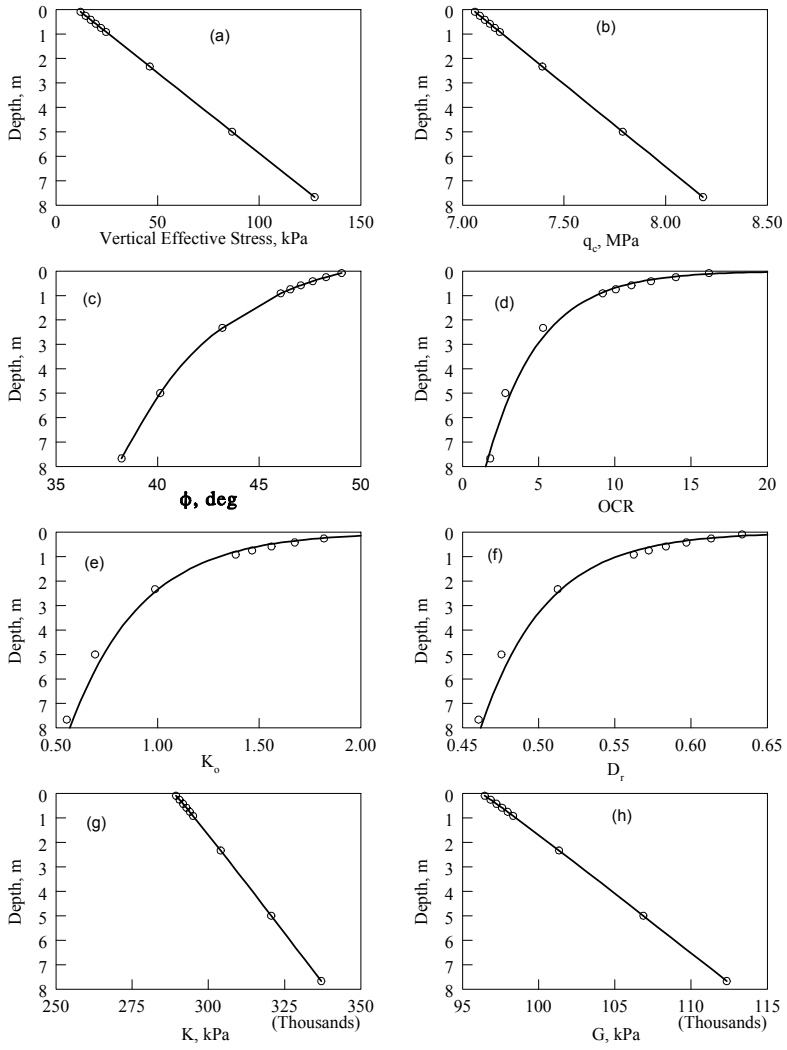

Figure C-1 Evaluation of cap model parameters from cone penetration test results

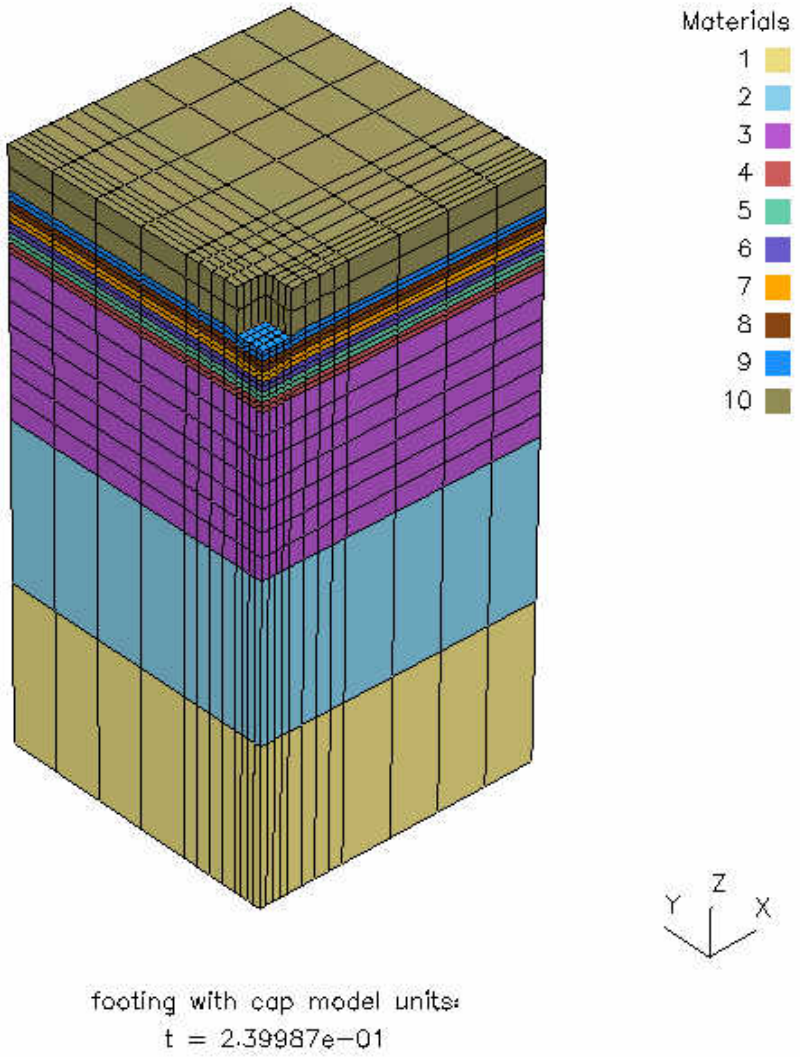

Figure C-2 Finite element discretization of Briaud and Gibbens' experiment

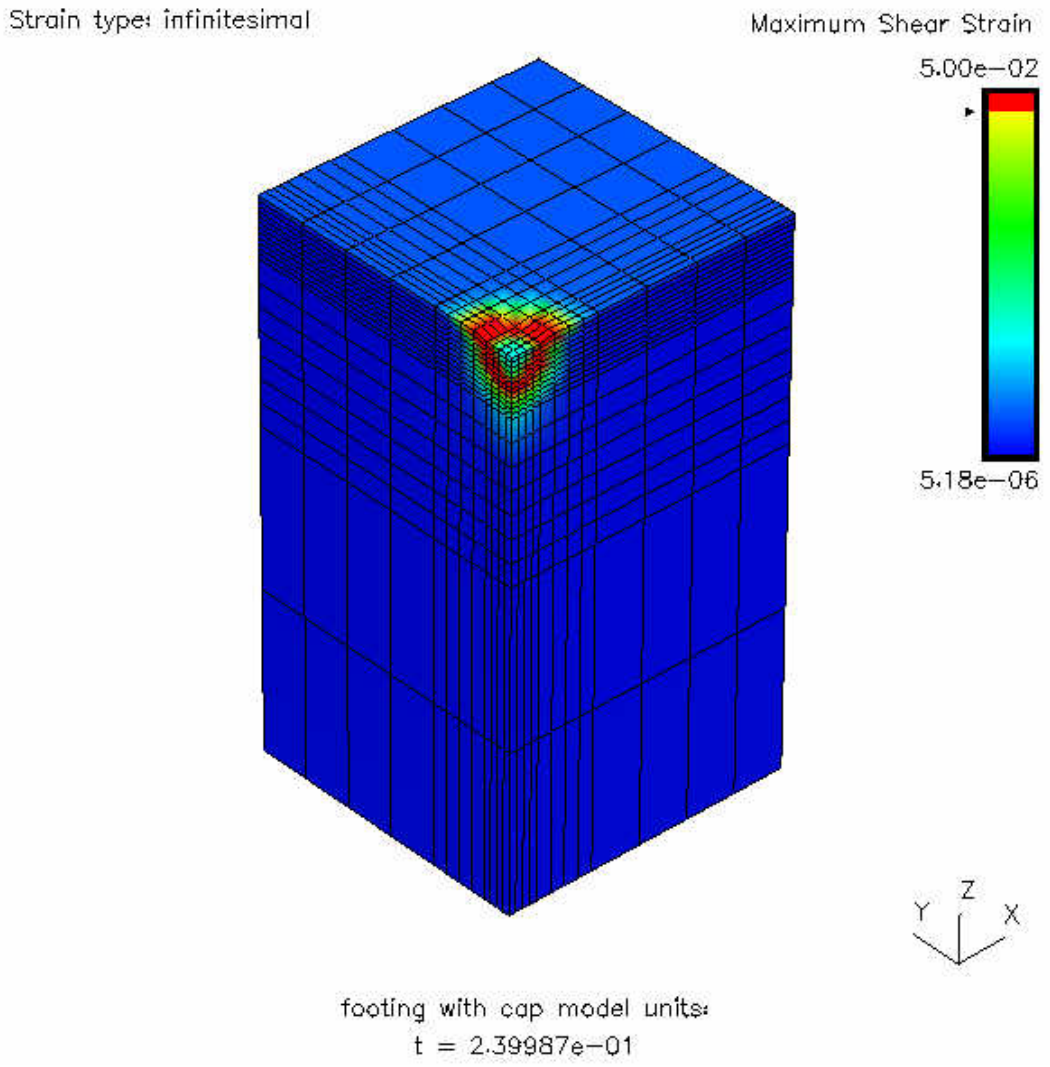

Figure C-3 Maximum shear strain distribution in soil

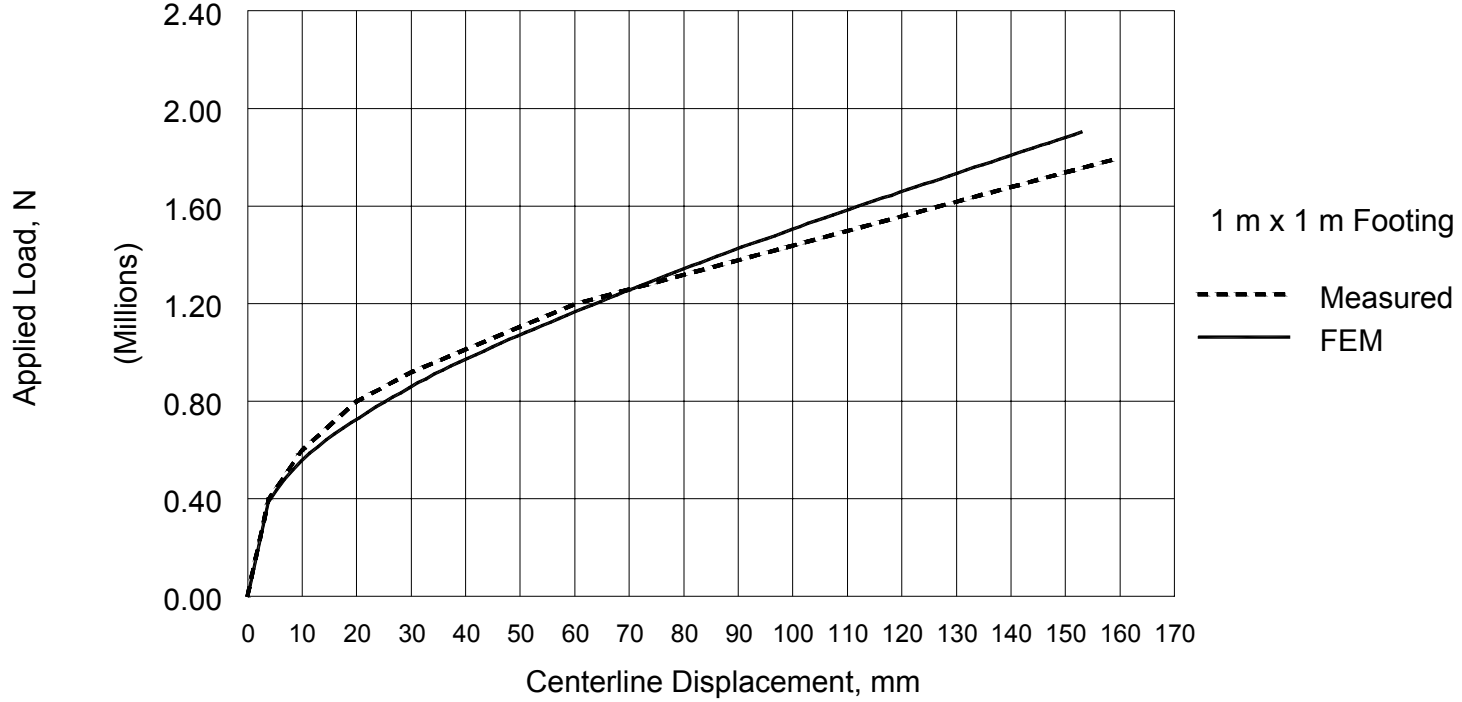

Figure C-4 Load-displacement curve for 1 m by 1 m footing: measured versus calculated

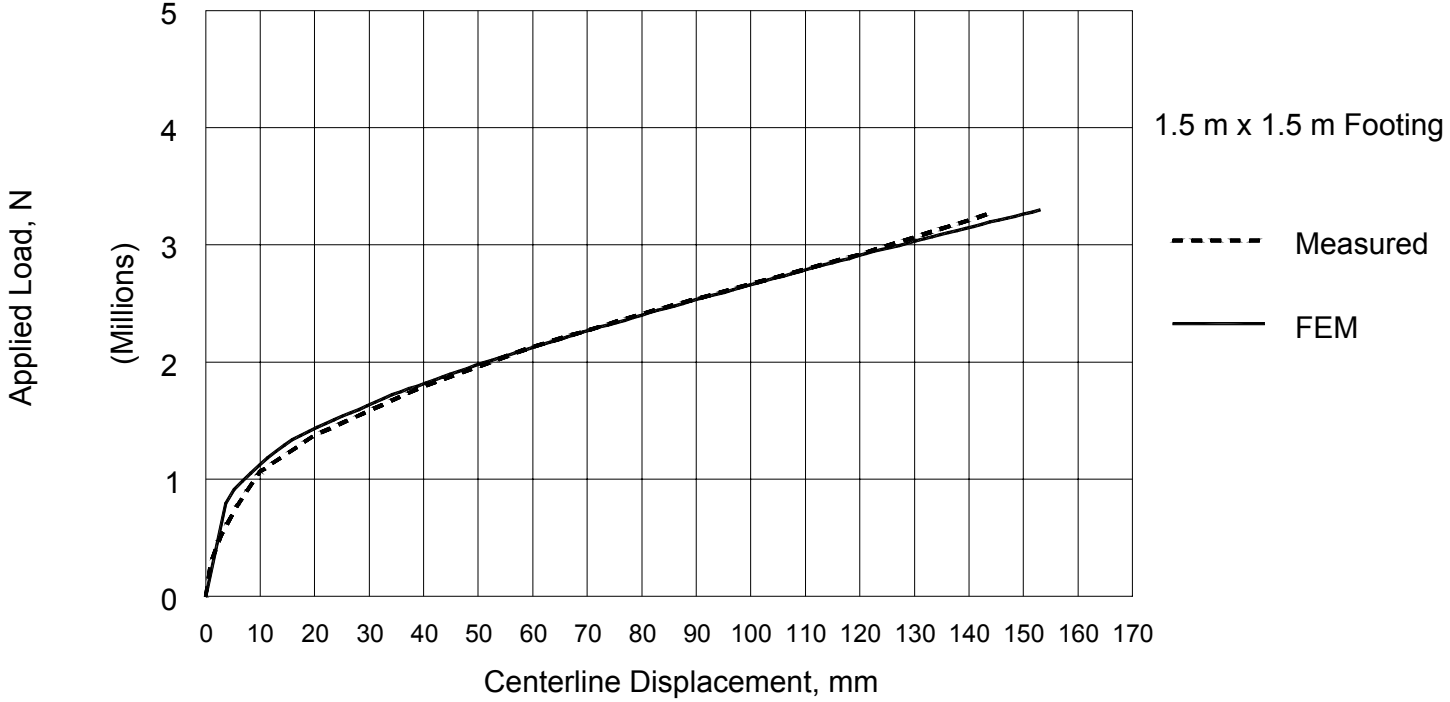

Figure C-5 Load-displacement curve for 1.5 m by 1.5 m footing: measured versus calculated

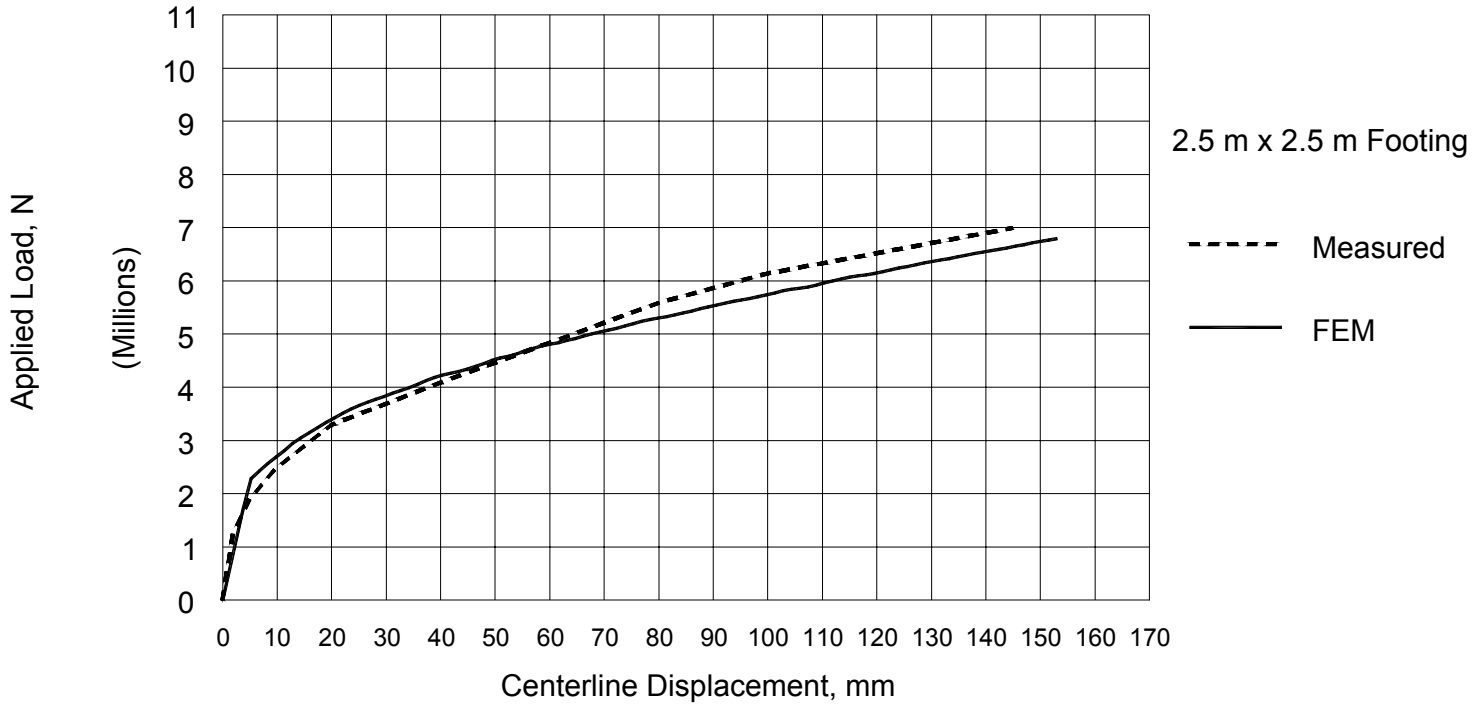

Figure C-6 Load-displacement curve for 2.5 m by 2.5 m footing: measured versus calculated

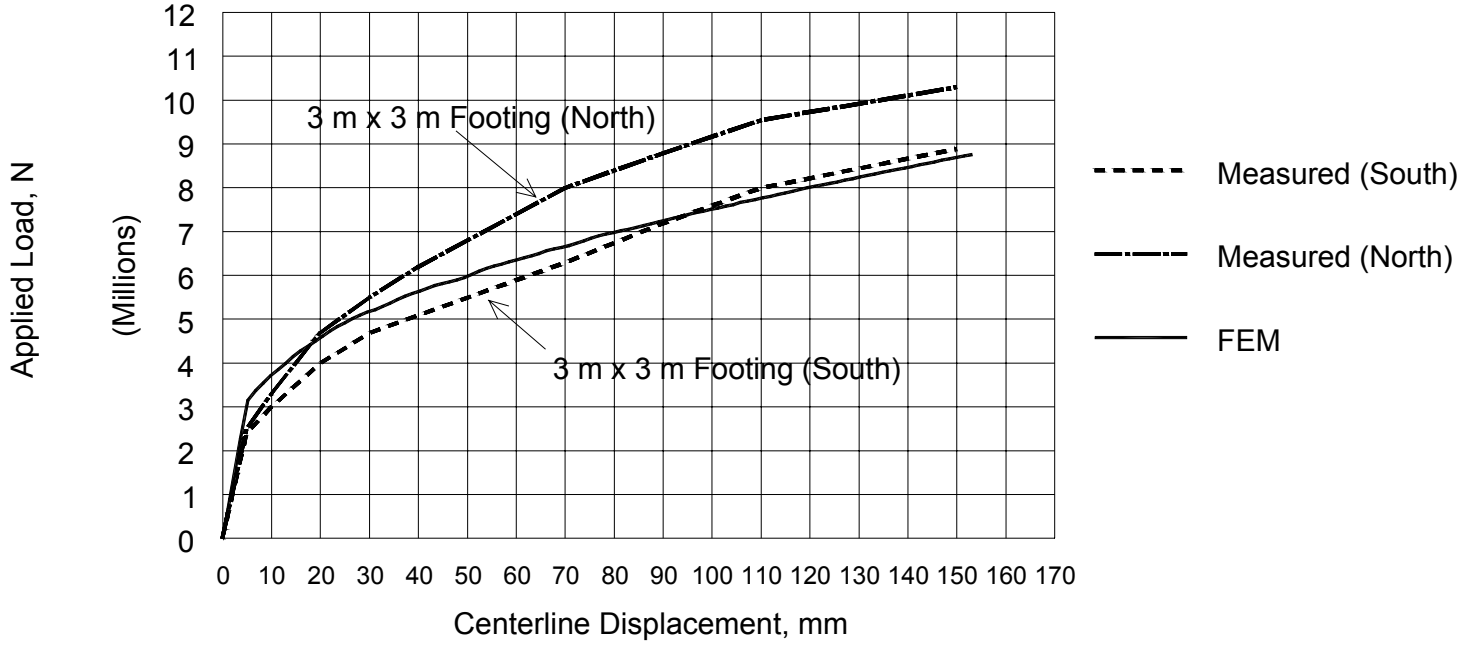

Figure C-7 Load-displacement curve for 3 m by 3 m footing: measured versus calculated

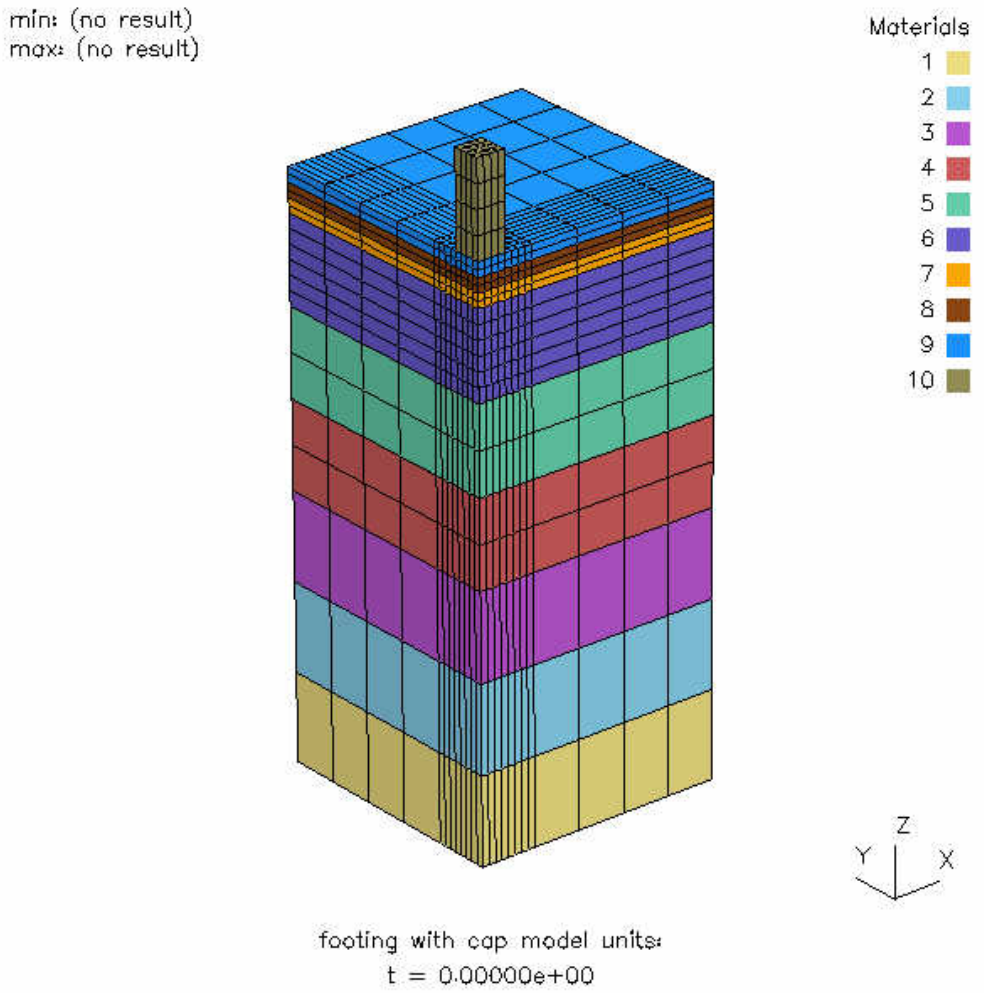

Figure C-8 Finite element discretization of Adams and Collin's spread footing experiment

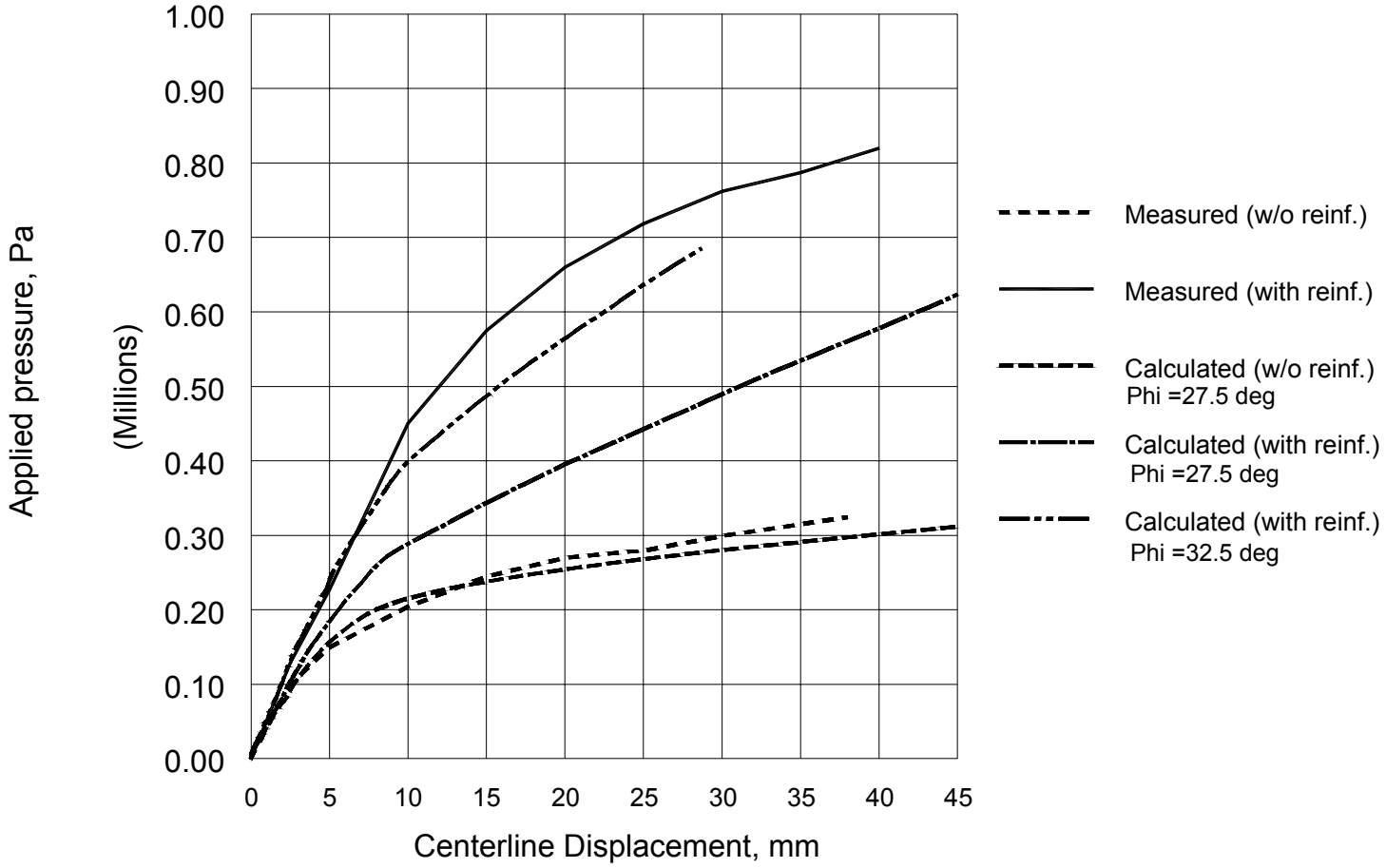

Figure C-9 Load-displacement curve for 0.61 m by 0.61 m footing with and without reinforcement

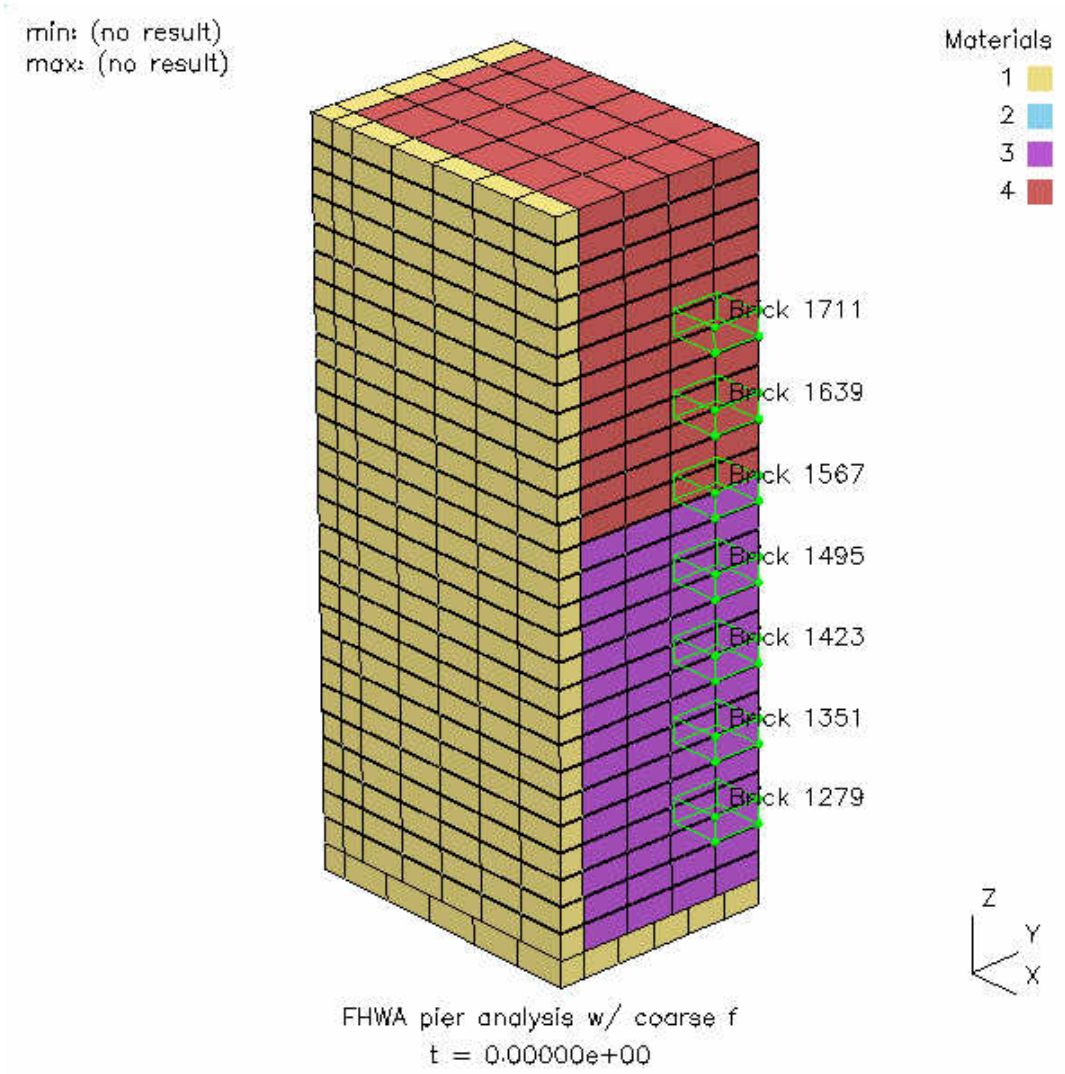

Figure C-10 Finite element discretization of the FHWA Pier: soil and segmental facing

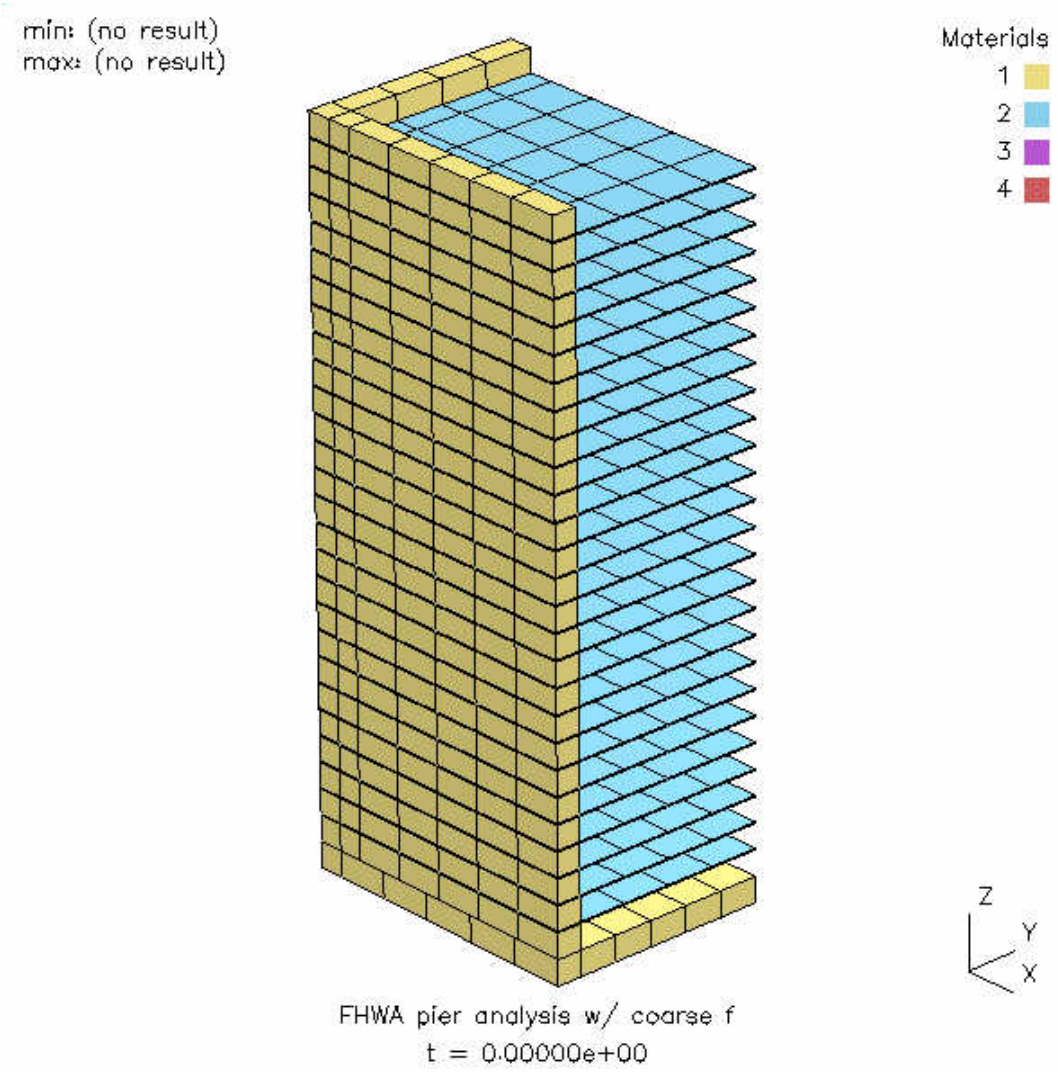

Figure C-11 Finite element discretization of the FHWA Pier: reinforcement and segmental facing

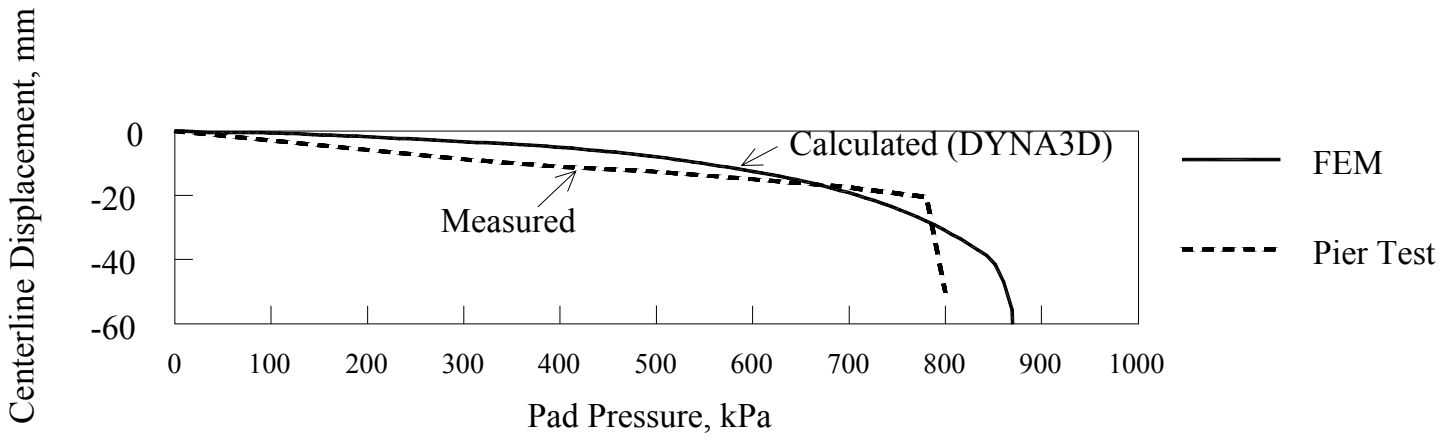

Figure C-12 Measured versus calculated load-displacement relationship of the FHWA Pier

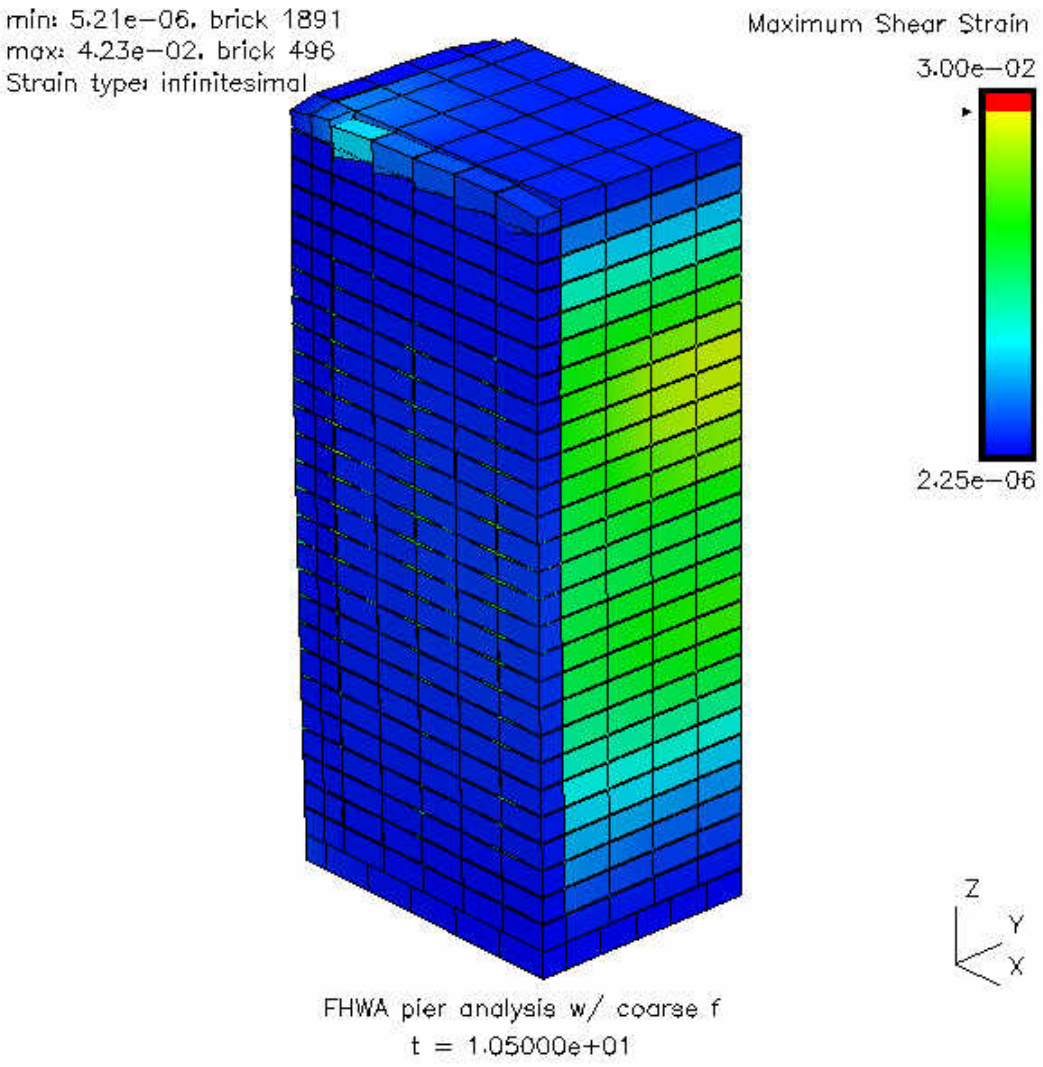

Figure C-13 Maximum shear strain distribution prior to failure

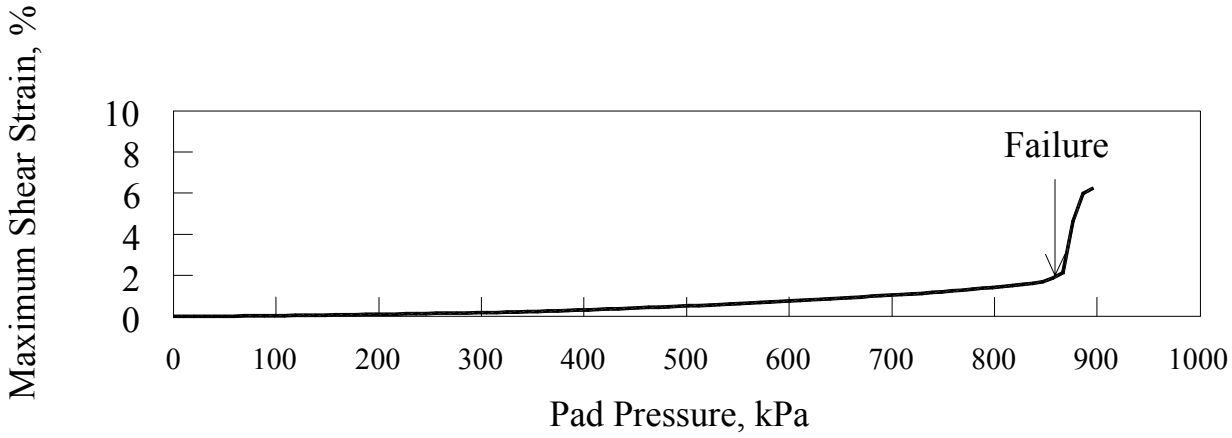

Figure C-14 Maximum shear strain vs. pad pressure relationship for selected soil elements

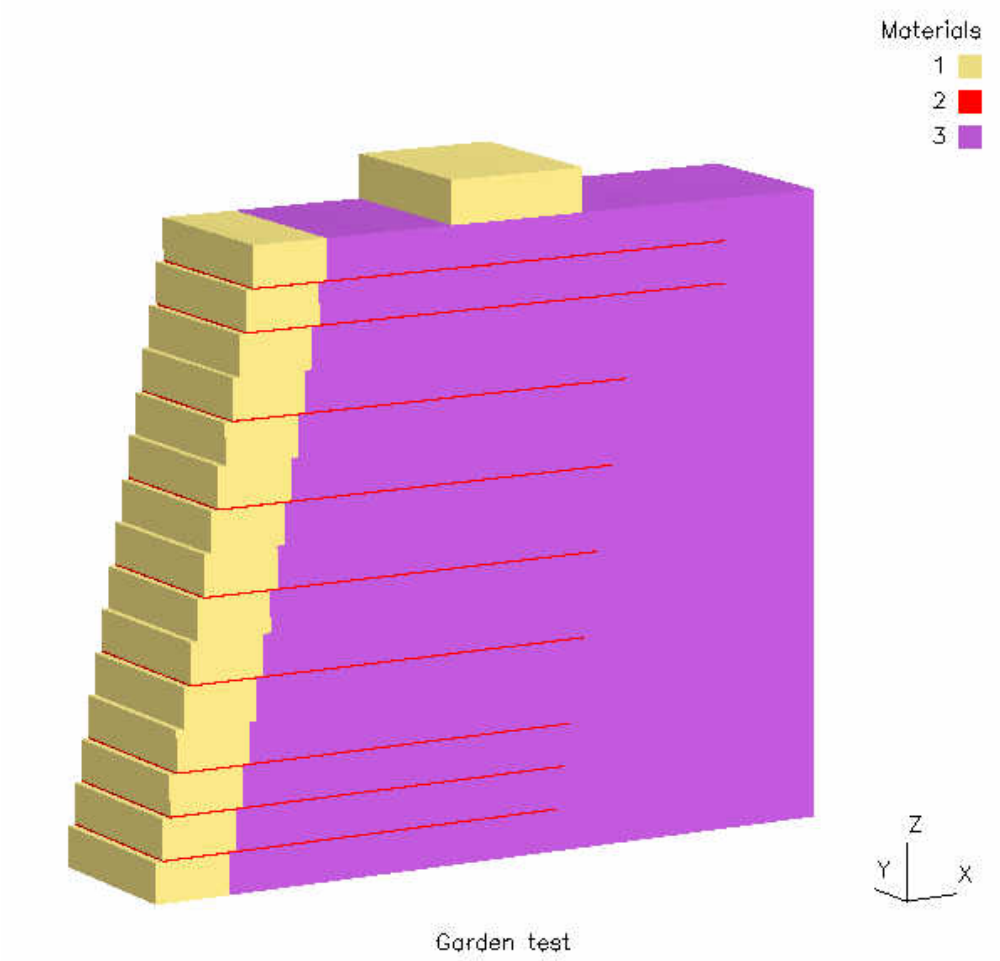

Figure C-15 Configuration of the "Garden" experiment

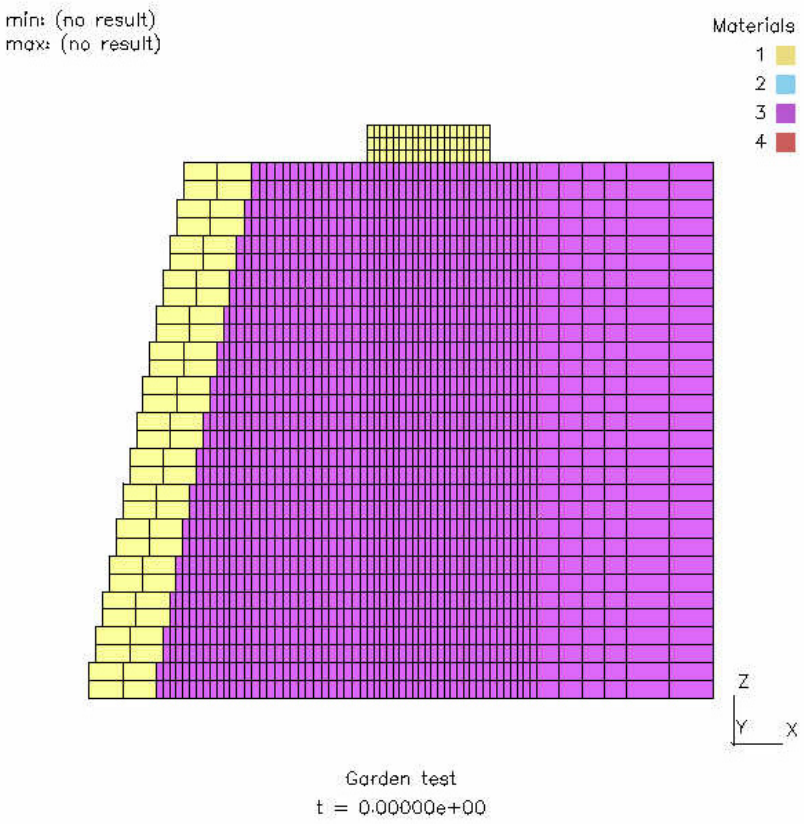

Figure C-16 Finite element discretization of the "Garden" experiment

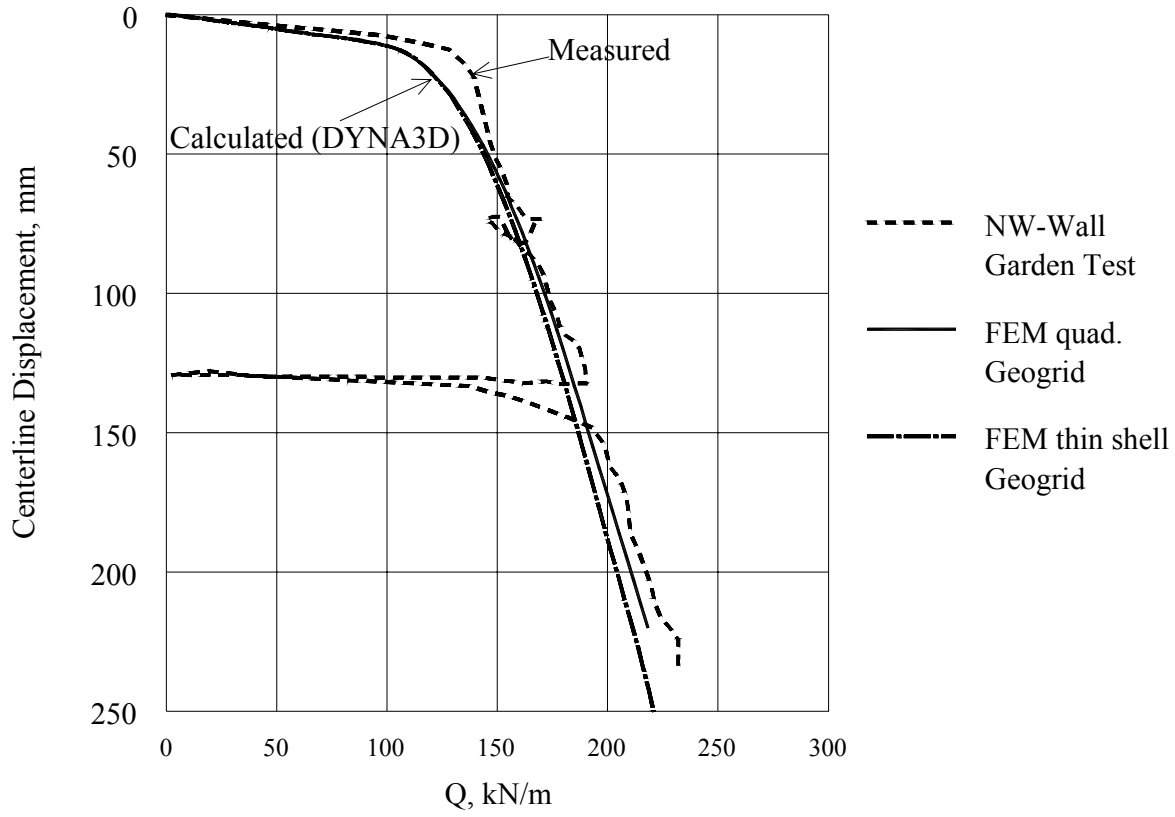

Figure C-17 Measured vs. calculated load-displacement relationships for the “Garden” experiment

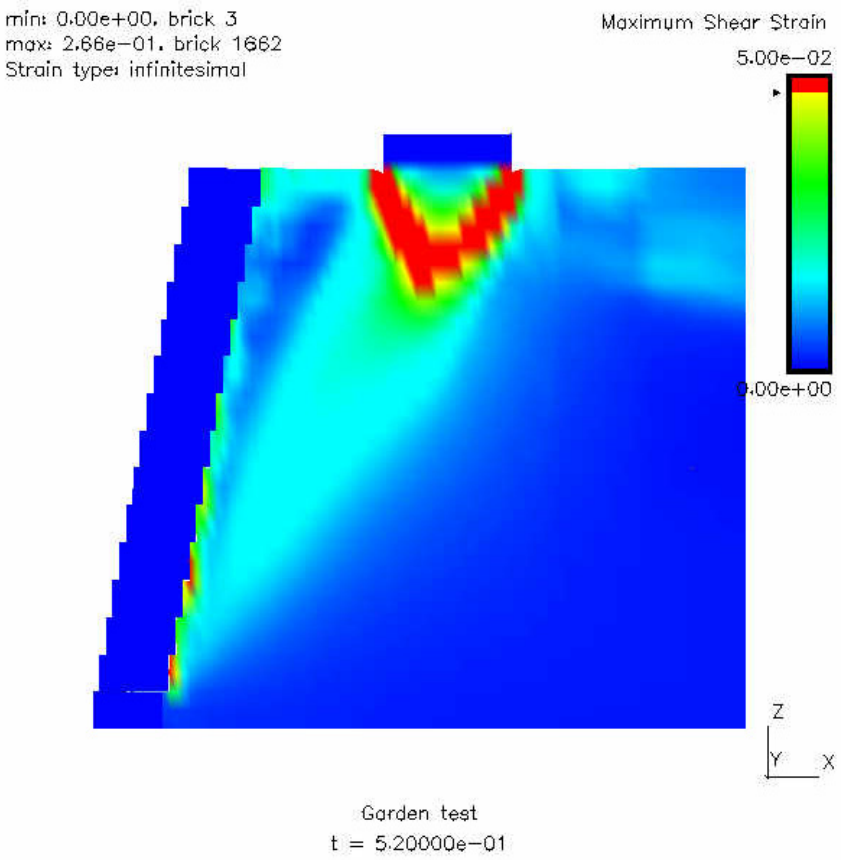

Figure C-18 Maximum shear strain distribution at failure pressure of 140 kPa

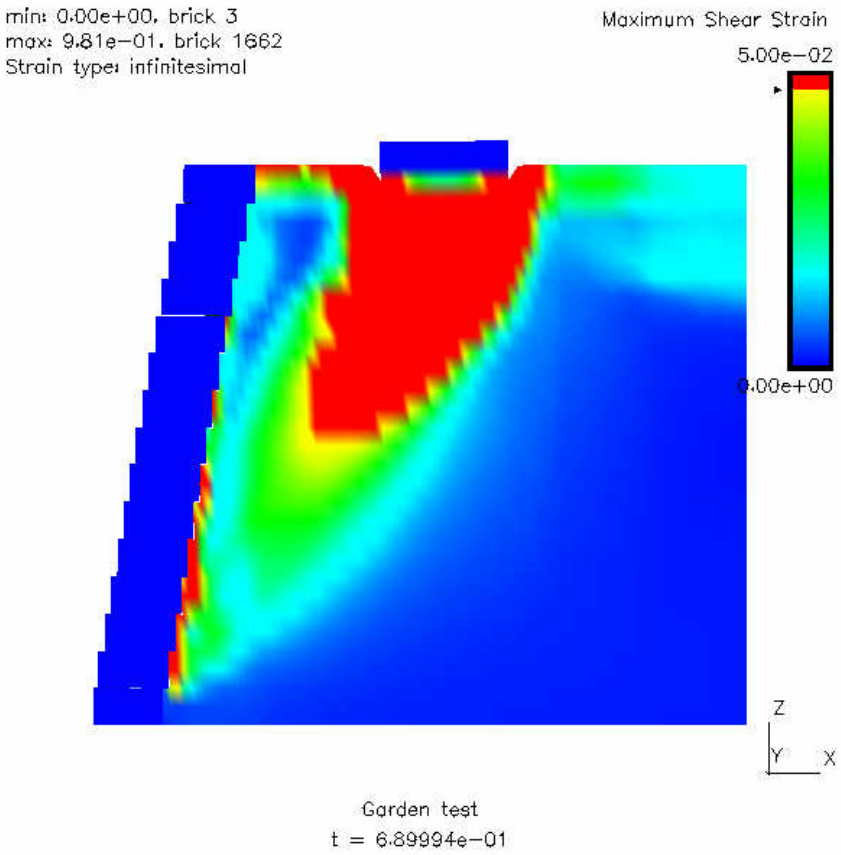

Figure C-19 Maximum shear strain distribution after failure (at 190 kPa)

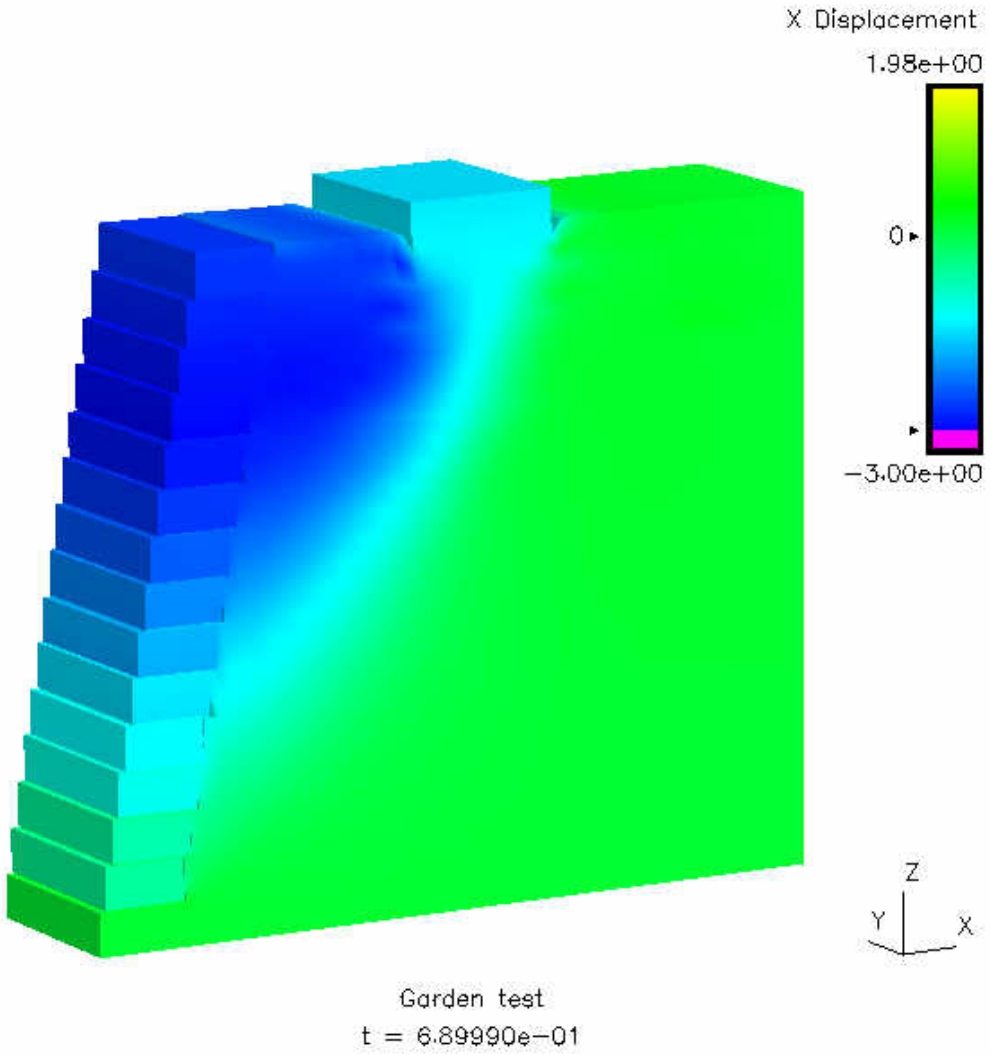

Figure C-20 Distribution of lateral displacement after failure (at 190 kPa)

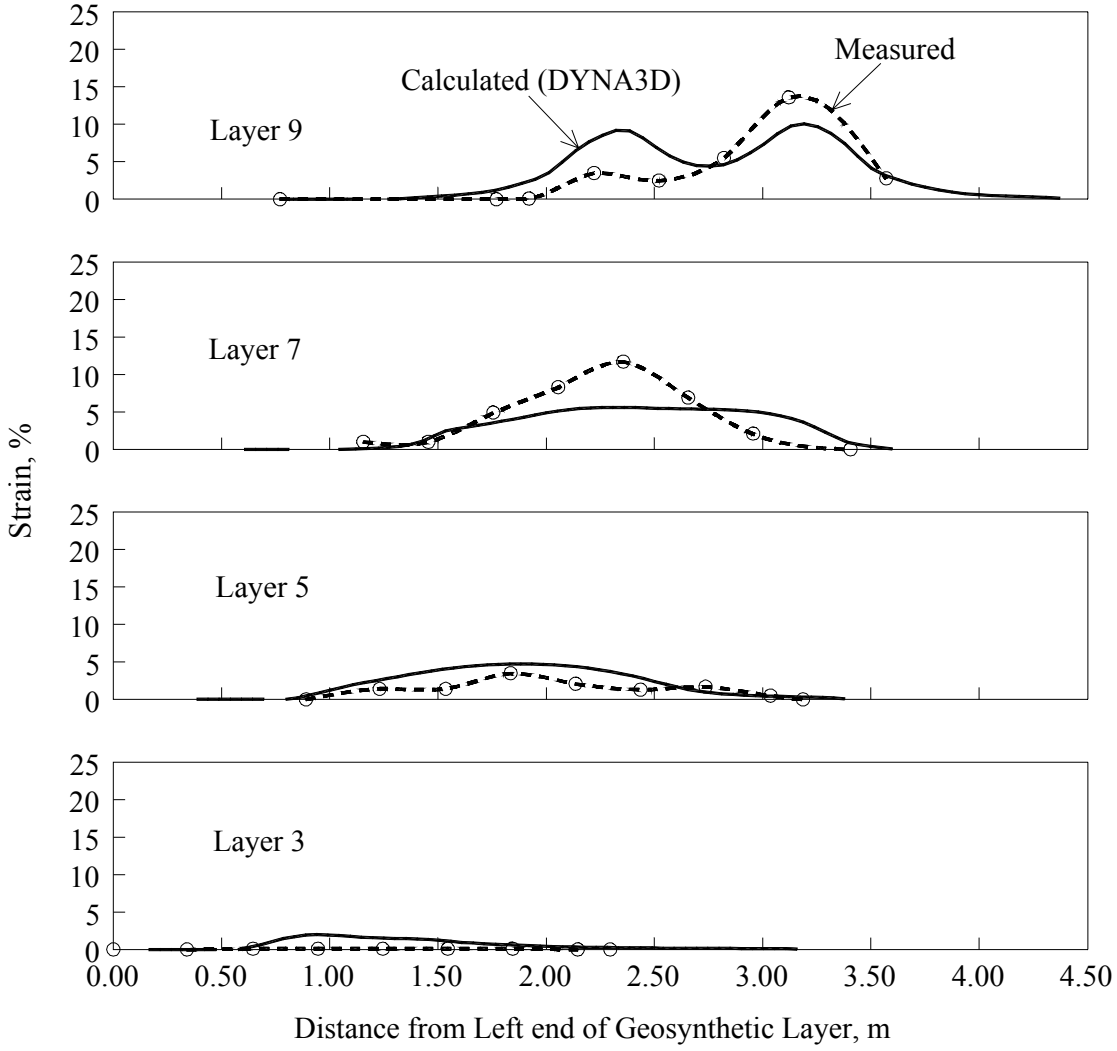

Figure C-21 Measured vs. calculated strains for geotextile layers 3, 5, 7, and 9

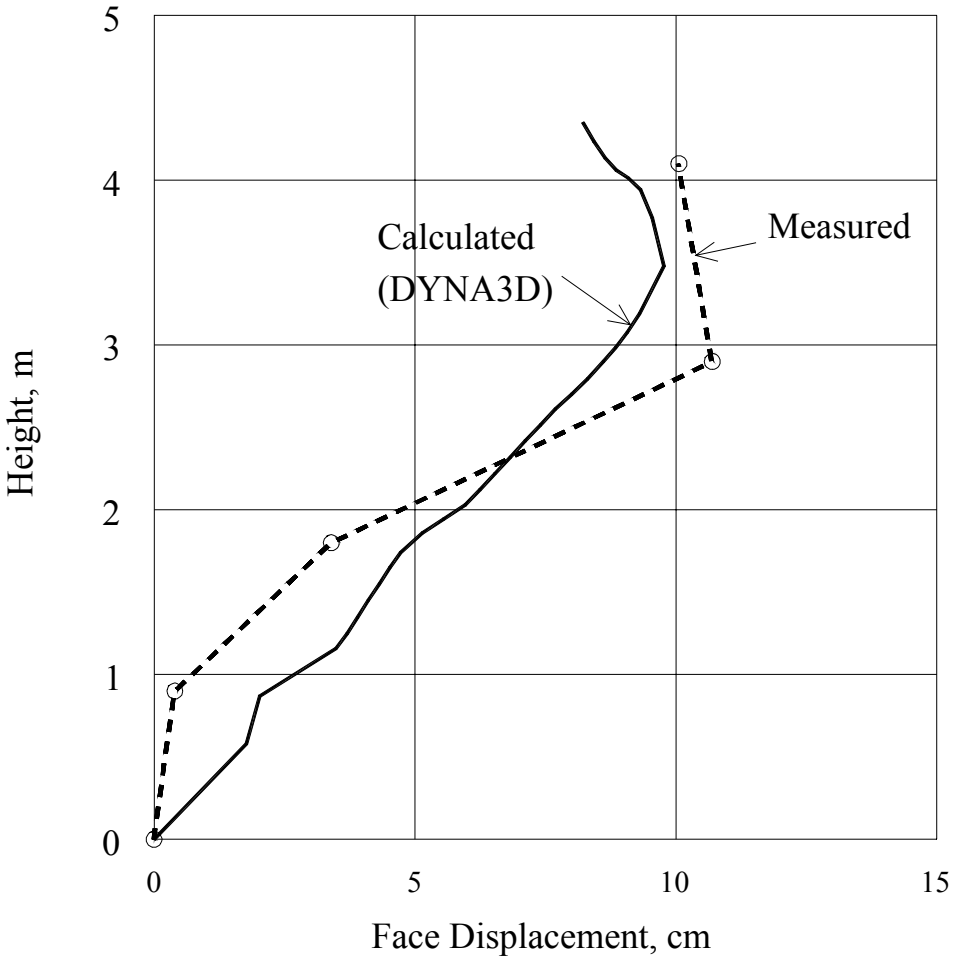

Figure C-22 Measured vs. calculated lateral displacements relationships of segmental facing

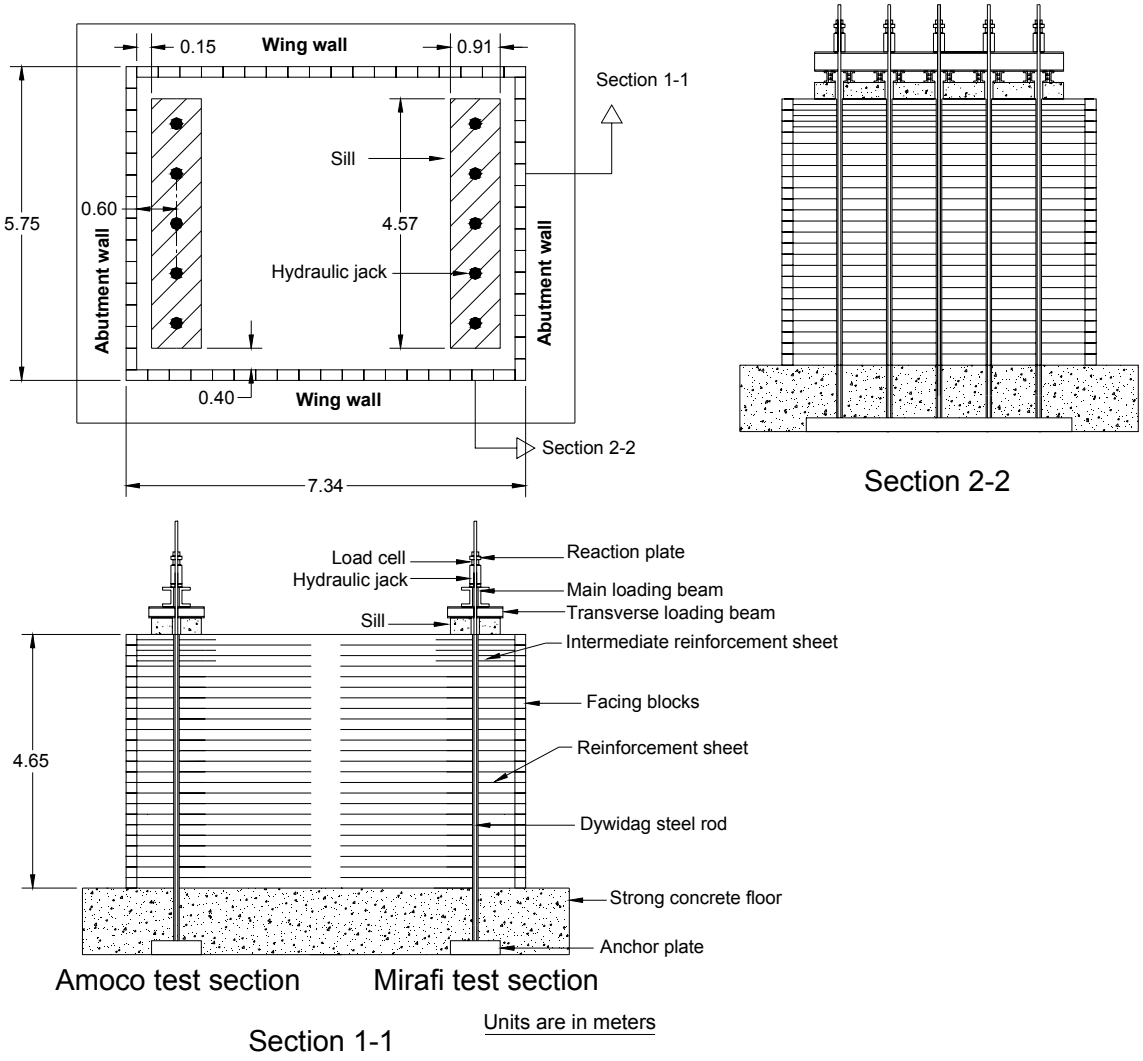

Figure C-23 Configuration of the NCHRP full-scale test abutments

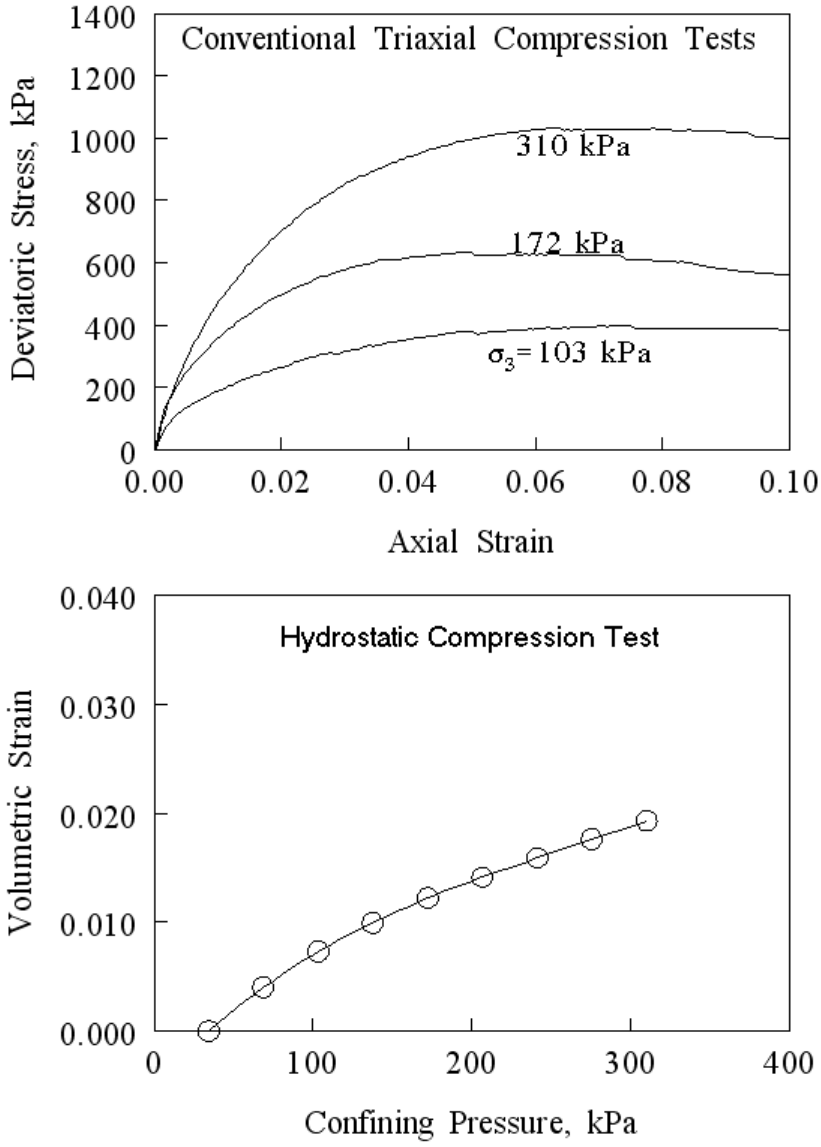

Figure C-24 Triaxial test results of the backfill

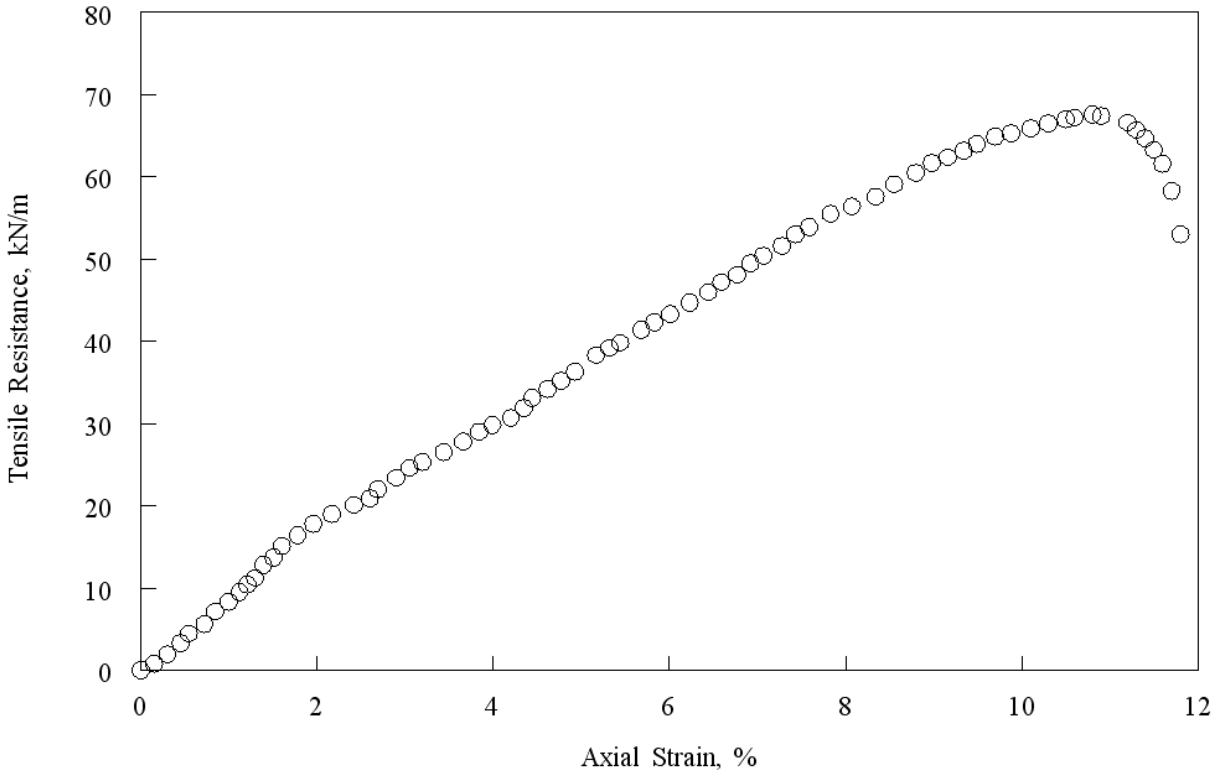

Figure C-25 Uniaxial tension test results of Amoco 2044 geotextile

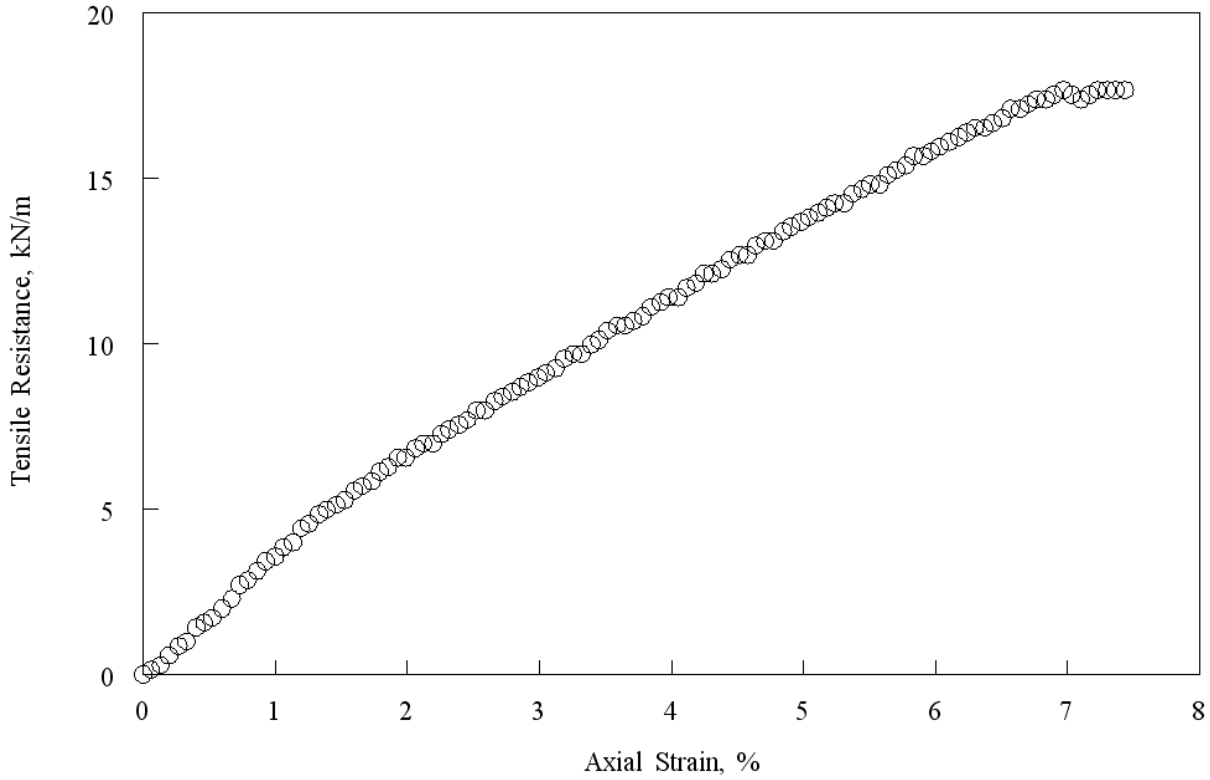

Figure C-26 Uniaxial tension test results of Mirafi 500x

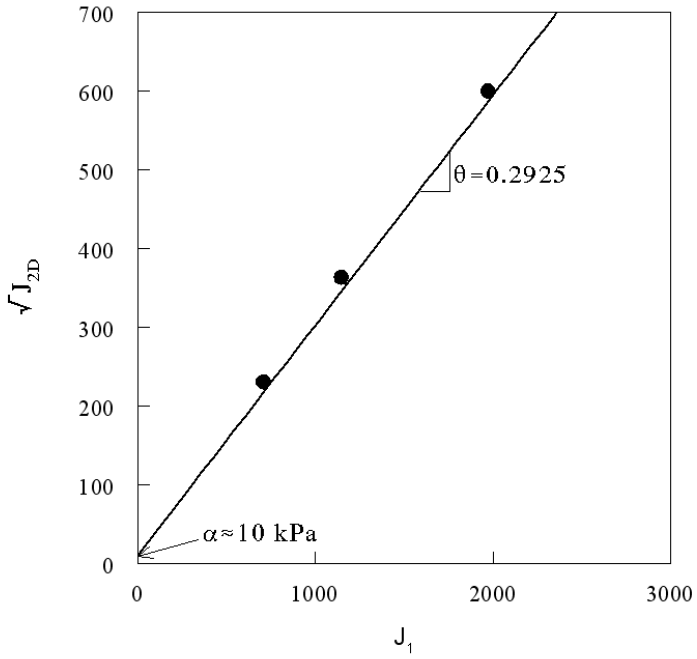

Figure C-27 Evaluation of the strength parameters, θ and α, for cap model from triaxial test results

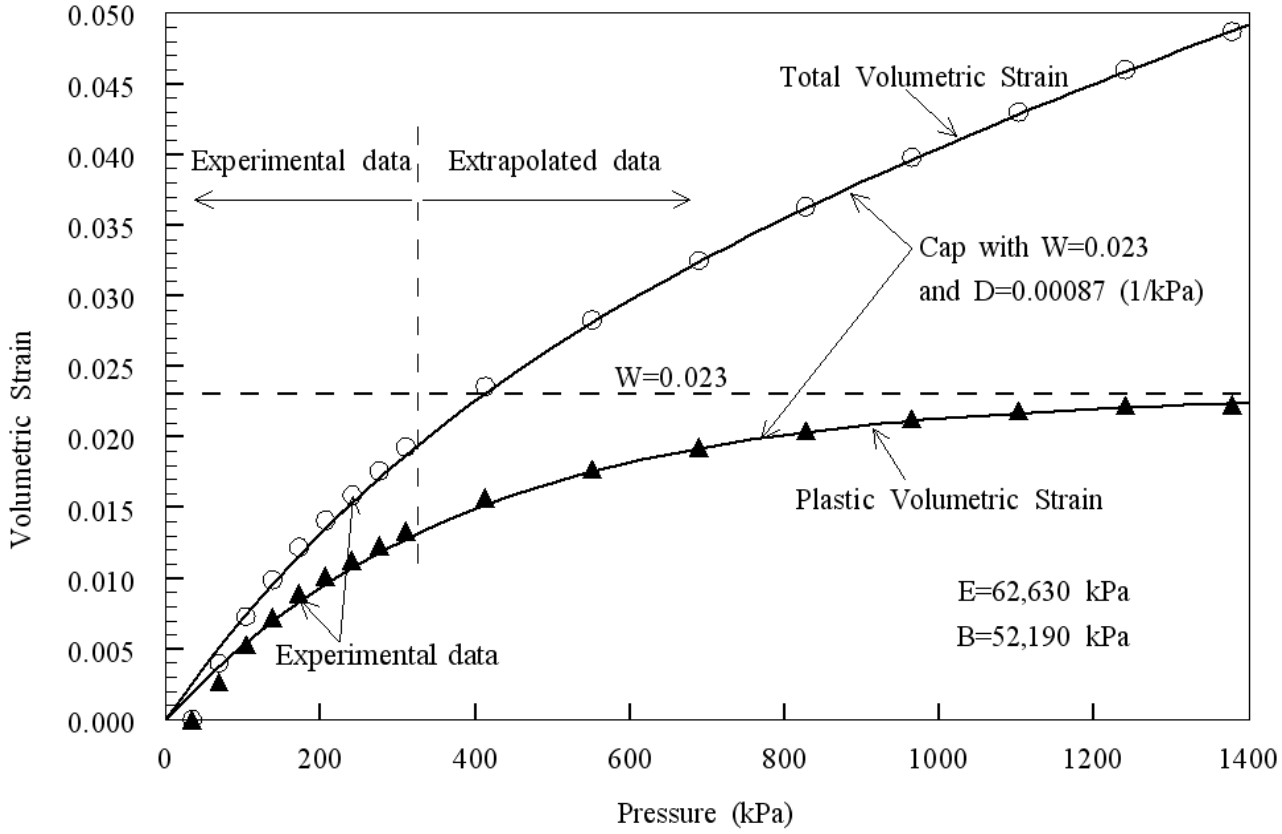

Figure C-28 Evaluation of the plastic potential Parameters, W and D, for cap model from hydrostatic compression test results

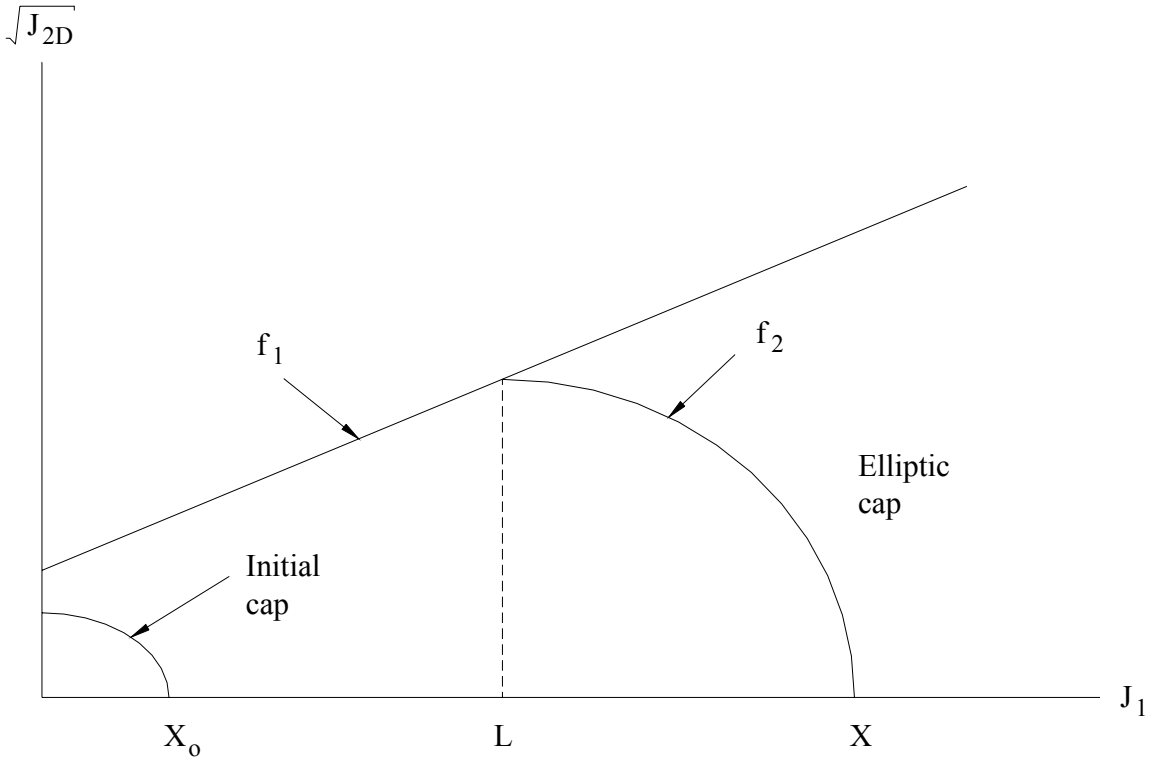

Figure C-29 The cap model

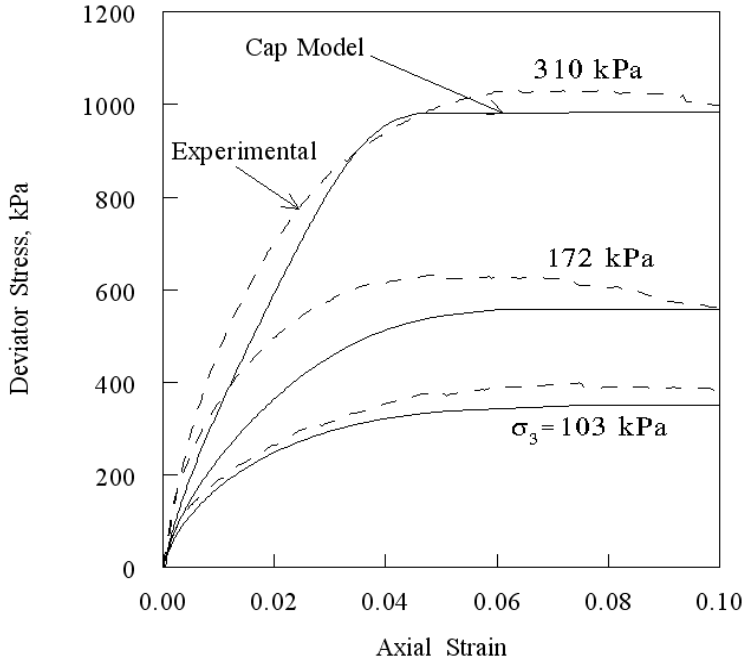

Figure C-30 Comparison between experimental and numerical soil behavior in triaxial compression

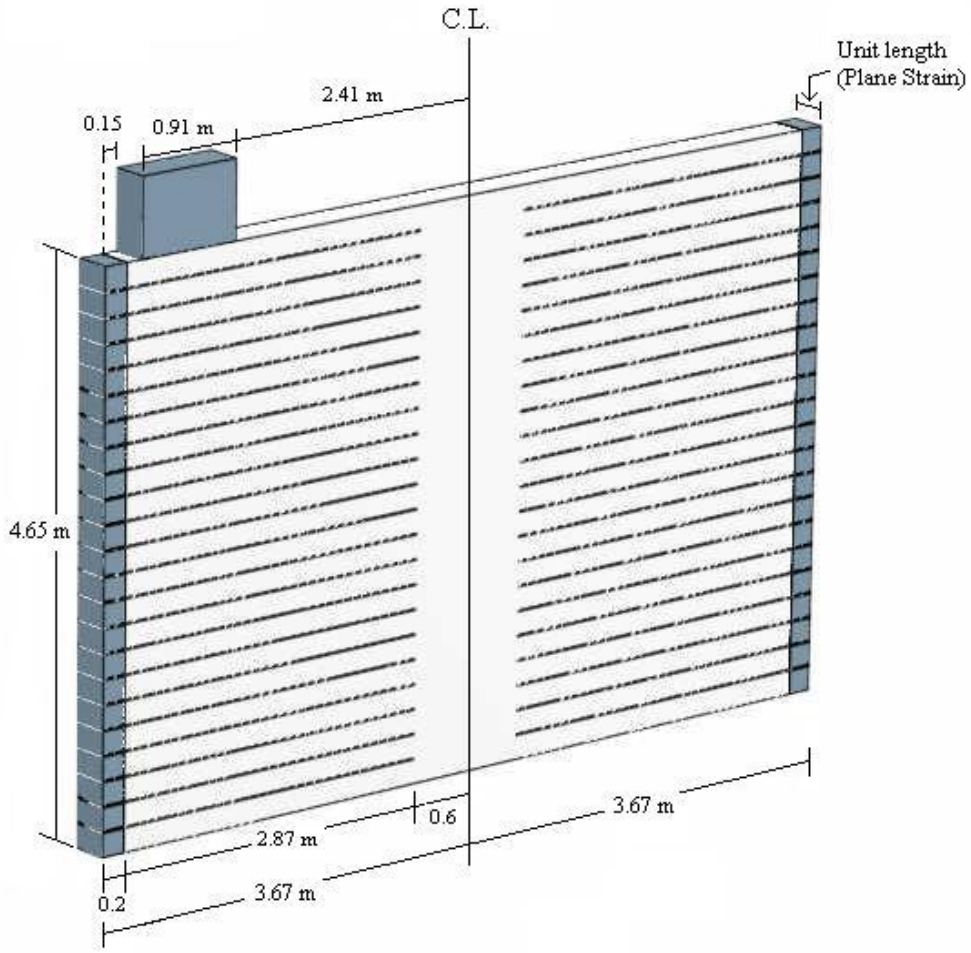

Figure C-31 GRS bridge abutment wall configuration

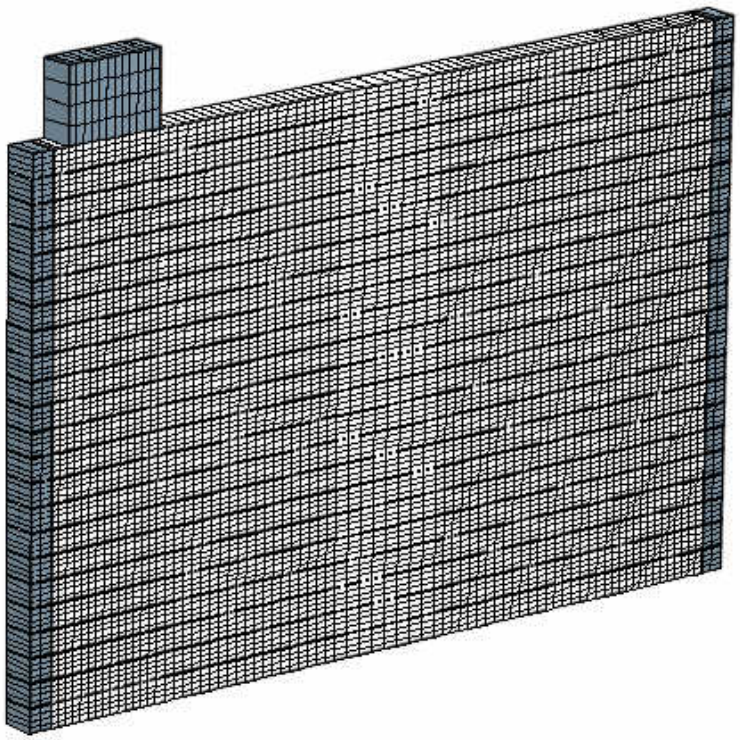

Figure C-32 Finite element mesh

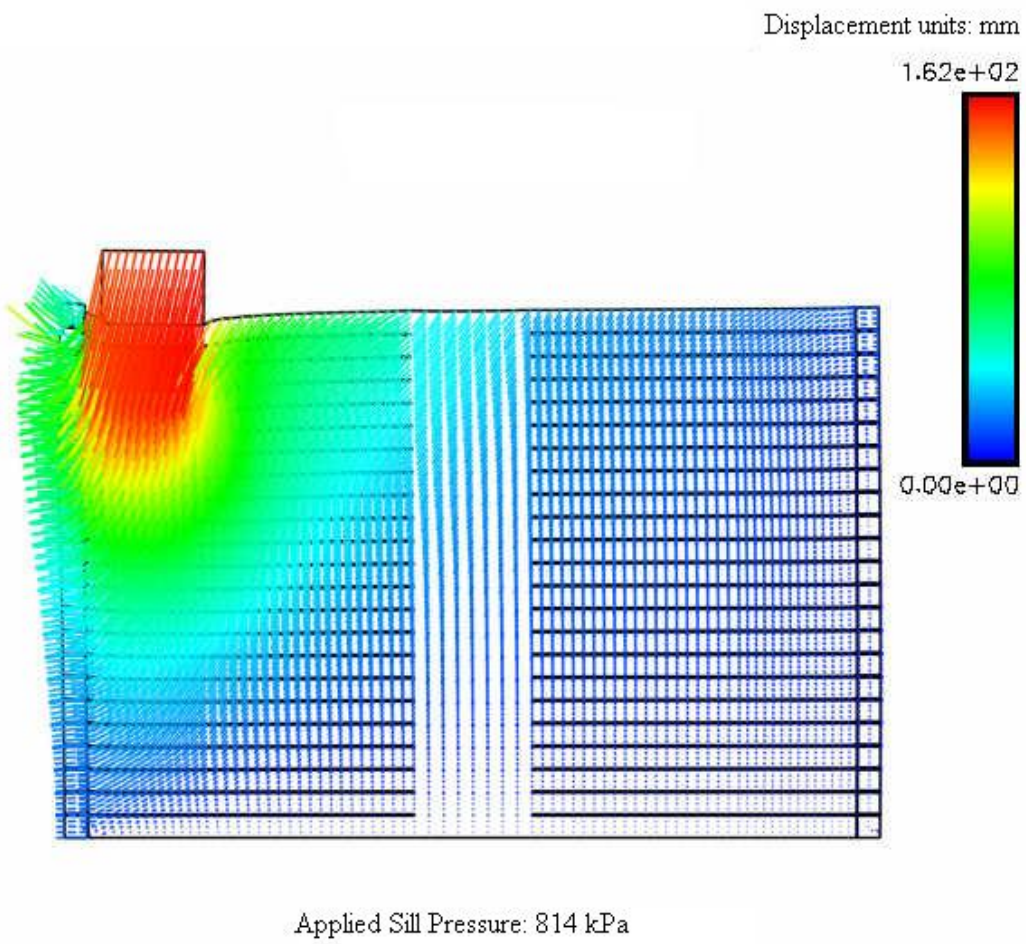

Figure C-33 Displacement field at sill pressure of 814 kPa (Amoco test section)

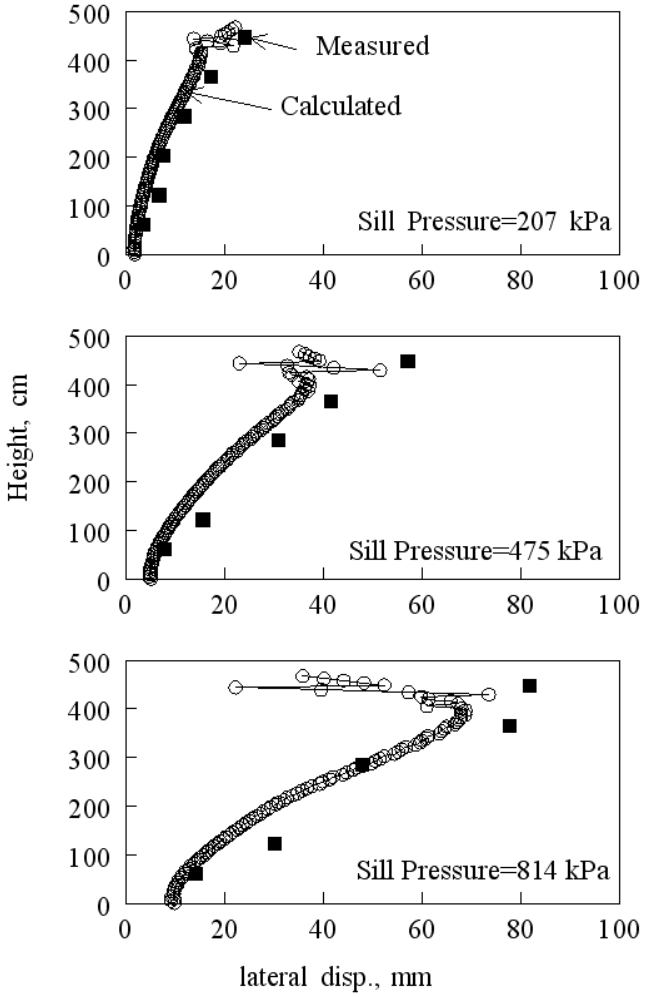

Figure C-34 Measured and calculated lateral displacements of facing (Amoco test section)

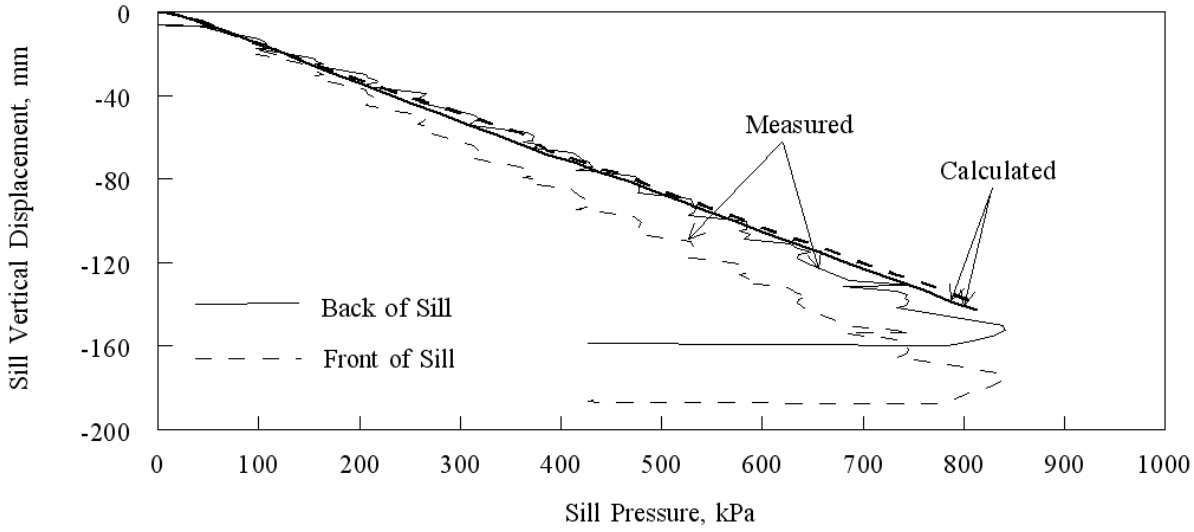

Figure C-35 Measured and calculated vertical displacements of sill (Amoco test section)

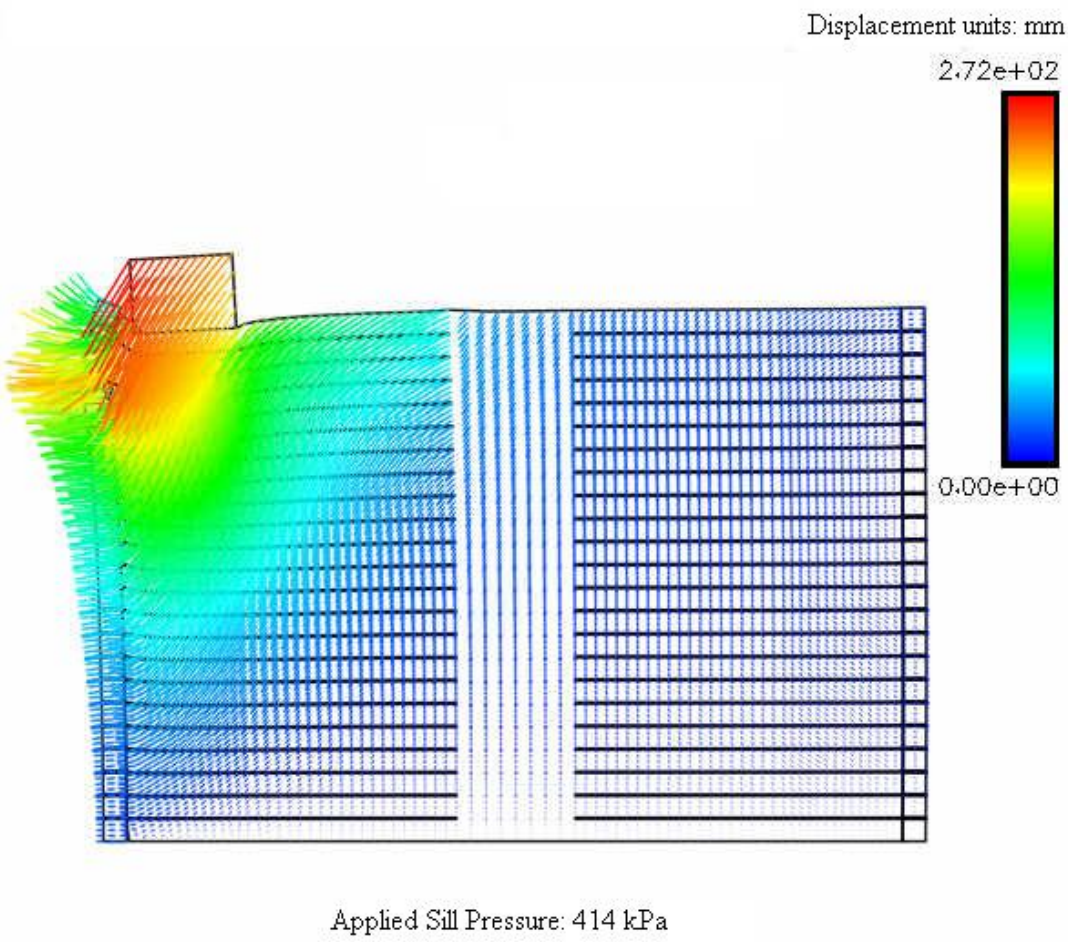

Figure C-36 Displacement field at sill pressure of 414 kPa (Mirafi test section)

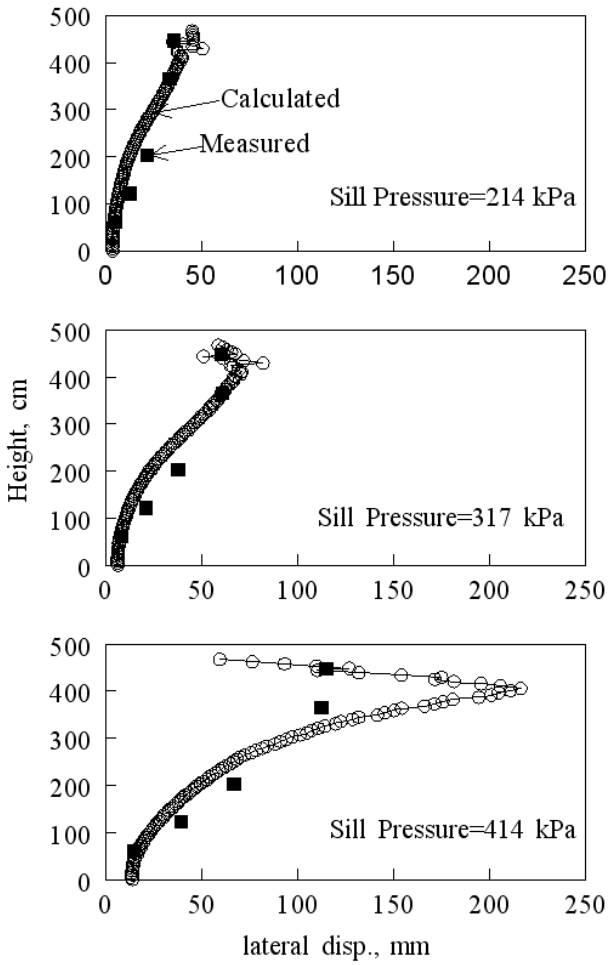

Figure C-37 Measured and calculated lateral displacements of facing (Mirafi test section)

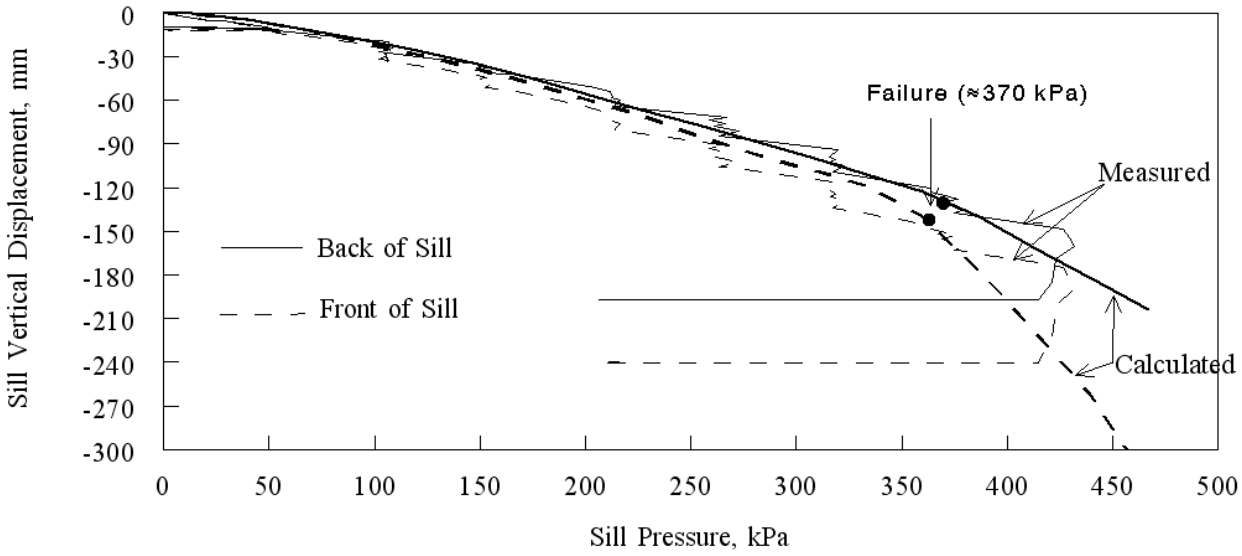

Figure C-38 Measured and calculated vertical displacements of sill (Mirafi test section)

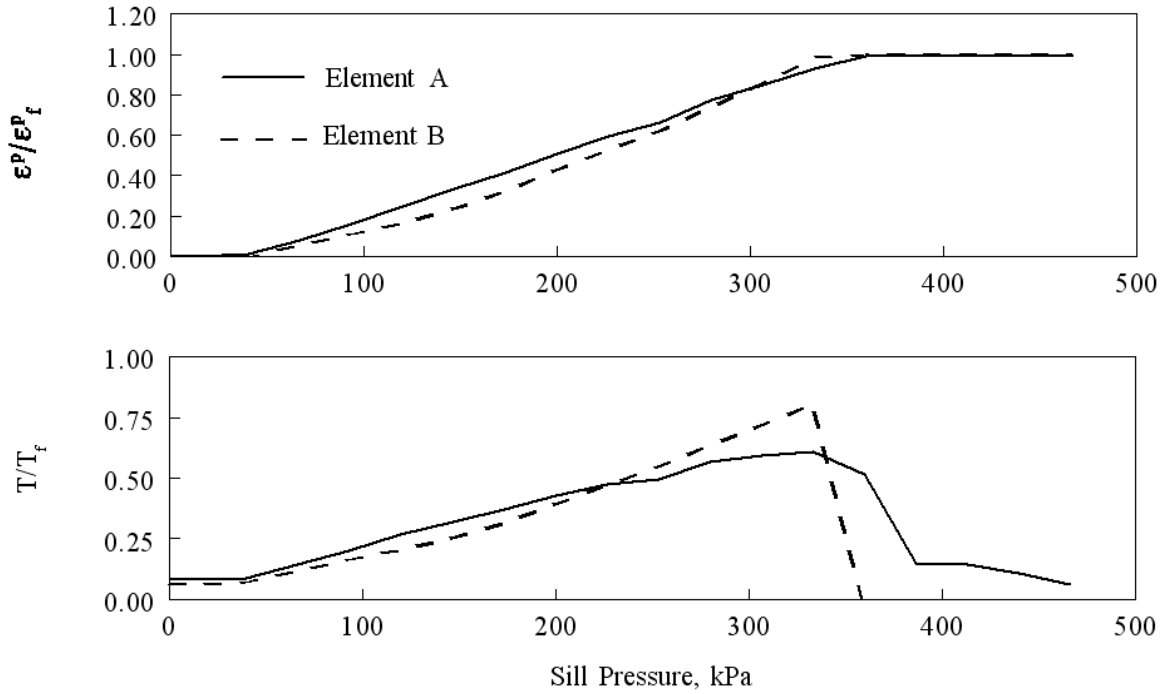

Figure C-39 Sample behavior of reinforcement (Elements A and B are located in the two uppermost reinforcement layers adjacent to facing blocks. Note the total loss of tensile capacity after reinforcement failure. Catastrophic wall failure immediately occurred after reinforcement failure.)